

Electronic Supplementary Material (ESI) for Energy & Environmental Science.
This journal is © The Royal Society of Chemistry 2017

Electronic Supplementary Information

Enhanced Photoelectrochemical Water Splitting of Hematite Multilayer Nanowires Photoanode with Tuning Surface State via Bottom-up Interfacial Engineering

PengYi Tang,^{a,b} HaiBing Xie,^a Carles Ros,^a LiJuan Han,^c Martí Biset-Peiró,^a YongMin He,^d Wesley Kramer,^e Alejandro Pérez Rodríguez,^a Edgardo Saucedo,^a José Ramón Galán-Mascarós,^{c,f} Teresa Andreu,^a Joan Ramon Morante,^a Jordi Arbiol^{b,f,*}

^a Catalonia Institute for Energy Research (IREC), Jardins de les Dones de Negre 1, Sant Adrià del Besòs, Barcelona 08930, Catalonia, Spain.

^b Catalan Institute of Nanoscience and Nanotechnology (ICN2), CSIC and The Barcelona Institute of Science and Technology (BIST), Campus UAB, Bellaterra, 08193 Barcelona, Catalonia, Spain.

^c Institute of Chemical Research of Catalonia (ICIQ), The Barcelona Institute of Science and Technology (BIST), Avinguda Paisos Catalans 16, Tarragona 43007, Catalonia, Spain.

^d School of Physical Science and Technology, Lanzhou University, Lanzhou 730000, China.

^e Beckman Institute and Division of Chemistry and Chemical Engineering, California Institute of Technology, 1200 East California Boulevard, Pasadena, California 91125, United States.

^f ICREA, Pg. Lluís Companys 23, 08010 Barcelona, Catalonia, Spain.

*Emails: arbiol@icrea.cat

CONTENTS

Figure S1. High resolution XPS spectra of C 1s, Sn 3d and In 3d of Fe ₂ O ₃ , ITO/Fe ₂ O ₃ , ITO/Fe ₂ O ₃ /Fe ₂ TiO ₅ , and ITO/Fe ₂ O ₃ /Fe ₂ TiO ₅ /FeNiOOH electrodes.....	(4)
Figures S2. (A): Grazing incidence XRD patterns of Fe ₂ O ₃ , ITO/Fe ₂ O ₃ , ITO/Fe ₂ O ₃ /Fe ₂ TiO ₅ , and ITO/Fe ₂ O ₃ /Fe ₂ TiO ₅ /FeNiOOH electrodes. (B): Absorptance of Fe ₂ O ₃ , ITO/Fe ₂ O ₃ , ITO/Fe ₂ O ₃ /Fe ₂ TiO ₅ , and ITO/Fe ₂ O ₃ /Fe ₂ TiO ₅ /FeNiOOH electrodes.....	(5)
Figure S3. EDS obtained on Fe ₂ O ₃ , ITO/Fe ₂ O ₃ , ITO/Fe ₂ O ₃ /Fe ₂ TiO ₅ , and ITO/Fe ₂ O ₃ /Fe ₂ TiO ₅ /FeNiOOHelectrodes.....	(6)
Figure S4. 1*1*1 unit crystal model of hematite, In ₂ O ₃ , Fe ₂ TiO ₅ and FeNiOOH create based on the crystal data in ICSD and reported data for the identification of the phase.....	(7)
Figure S5. Low magnification TEM images of Fe ₂ O ₃ electrode.....	(8)
Figure S6-S7. TEM images of ITO/Fe ₂ O ₃ electrode.	(9-10)
Figure S8-S9. TEM images of ITO/Fe ₂ O ₃ /Fe ₂ TiO ₅ electrode.	(11)
Figure S10. TEM images of ITO/Fe ₂ O ₃ /Fe ₂ TiO ₅ /FeNiOOH electrode.....	(12)
Figure S11-S12. STEM-EELS chemical composition maps of Fe ₂ O ₃ electrode.....	(13-14)
Figure S13-S14. STEM-EELS chemical composition maps of the ITO/Fe ₂ O ₃ electrode.....	(15)
Figure S15-S16. STEM-EELS chemical composition maps of the ITO/Fe ₂ O ₃ /Fe ₂ TiO ₅ electrode.(16)	
Figure S17. STEM-EELS chemical composition maps of the ITO/Fe ₂ O ₃ /Fe ₂ TiO ₅ /FeNiOOH electrode.....	(17)
Figure S18. SEM images of the pristine FTO substrate, ITO-105 nm, ITO-245 nm, ITO-105 nm-Fe ₂ O ₃ and ITO-245 nm-Fe ₂ O ₃ electrodes.....	(18)
Figure S19. Top: the atomic model for optimized ITO/Fe ₂ O ₃ electrodes. Bottom: Left: CV curves of the ITO/Fe ₂ O ₃ electrodes with different ITO thickness sintering on 750 °C for 30min under illumination; Right: the photocurrent density at 1.23 V vs. RHE related to the ITO thickness.	(19)
Figure S20. SEM images of the ITO/Fe ₂ O ₃ /Fe ₂ TiO ₅ electrodes with different ALD cycles (TiO ₂ thickness), e.g. 15 cycles, 30 cycles, 50 cycles, 100 cycles and 150 cycles.....	(20)
Figure S21. Top: the atomic model for optimized ITO/Fe ₂ O ₃ /Fe ₂ TiO ₅ electrodes. Bottom: Left: CV curves of the ITO/Fe ₂ O ₃ /Fe ₂ TiO ₅ electrodes with different ALD TiO ₂ cycles (thickness) sintering on 750 °C for 30 min under illumination; Right: the photocurrent density at 1.23 V vs. RHE related to the ALD TiO ₂ cycles.....	(21)
Figure S22. SEM images of the ITO/Fe ₂ O ₃ /Fe ₂ TiO ₅ -30 cycles electrodes with different sintering time at 750°C, e.g. 10 min, 30 min, 40 min and 80 min.....	(22)
Figure S23. Top: the atomic model for optimized ITO/Fe ₂ O ₃ /Fe ₂ TiO ₅ electrodes. Bottom: Left: CV curves of the ITO/Fe ₂ O ₃ /Fe ₂ TiO ₅ -30 cycles electrodes with different sintering time on 750 °C under illumination; Right: the photocurrent density at 1.23 V vs. RHE related to the sintering time.....	(23)
Figure S24. SEM images of the ITO/Fe ₂ O ₃ /Fe ₂ TiO ₅ /FeNiOOH electrodes with different FeNiOOH deposition charge.....	(24)
Figure S25. Top: the atomic model for optimized ITO/Fe ₂ O ₃ /Fe ₂ TiO ₅ /FeNiOOH electrode. Bottom: Left: CV curves of the ITO/Fe ₂ O ₃ /Fe ₂ TiO ₅ /FeNiOOH electrodes with different FeNiOOH deposition charge under illumination; Right: the photocurrent density at 1.23 V vs. RHE related to the FeNiOOH deposition charge.....	(25)
Figure S26. SEM images of the Fe ₂ O ₃ /Fe ₂ TiO ₅ -30 cycles electrodes with different sintering time at 750 °C, e.g. 10 min, 30min, 1 h and 2 h.....	(26)

Figure S27. Top: the atomic model for optimized Fe₂O₃/Fe₂TiO₅-30 cycles electrode. Bottom: Left: CV curves of the Fe₂O₃/Fe₂TiO₅-30 cycles electrodes with different sintering conditions under illumination; Right: the photocurrent density at 1.23 V vs. RHE related to the sintering conditions.....(27)

Schematic S1. A: Equivalent circuit (EC) for the charge transfer process of hematite composite under illumination. B: simple Randles circuit for the charge transfer process of hematite composite under dark.....(28)

Figure S28. Nyquist (Imaginary vs. Real component of impedance) plots under light illumination of Fe₂O₃, ITO/Fe₂O₃, ITO/Fe₂O₃/Fe₂TiO₅, and ITO/Fe₂O₃/Fe₂TiO₅/FeNiOOH electrodes.....(29)

Figure S29. Nyquist (Imaginary vs. Real component of impedance) plots in the dark of Fe₂O₃, ITO/Fe₂O₃, ITO/Fe₂O₃/Fe₂TiO₅, and ITO/Fe₂O₃/Fe₂TiO₅/FeNiOOH electrodes.....(30)

Figure S30. C_{bulk} of Fe₂O₃, ITO/Fe₂O₃, ITO/Fe₂O₃/Fe₂TiO₅, and ITO/Fe₂O₃/Fe₂TiO₅/FeNiOOH electrodes under 1 sun illumination.....(31)

Figure S31. Mott-Schottky plots (C⁻² vs. E) of Fe₂O₃, ITO/Fe₂O₃, ITO/Fe₂O₃/Fe₂TiO₅, and ITO/Fe₂O₃/Fe₂TiO₅/FeNiOOH electrodes.(32)

Table S1. Flat band potential values (E_{fb}), bulk donor densities (N_d) and total surface state density (N_{ss}) of the Fe₂O₃, ITO/Fe₂O₃, ITO/Fe₂O₃/Fe₂TiO₅, and ITO/Fe₂O₃/Fe₂TiO₅/FeNiOOH electrodes.....(32)

Figure S32. SEM images of FeOOH nanowires on FTO substrate.....(33)

Figure S33. SEM images of FeOOH nanowires on FTO substrate after sintering at 550°C for 2h.....(33)

Schematic S2 The sample preparation process of FTO/ITO/Fe₂O₃/Fe₂TiO₅/FeNiOOH electrode for TEM and STEM-EELS characterization.....(34)

Table S2. Photo-electrochemical performance comparison of hematite based electrodes.....(35)

References

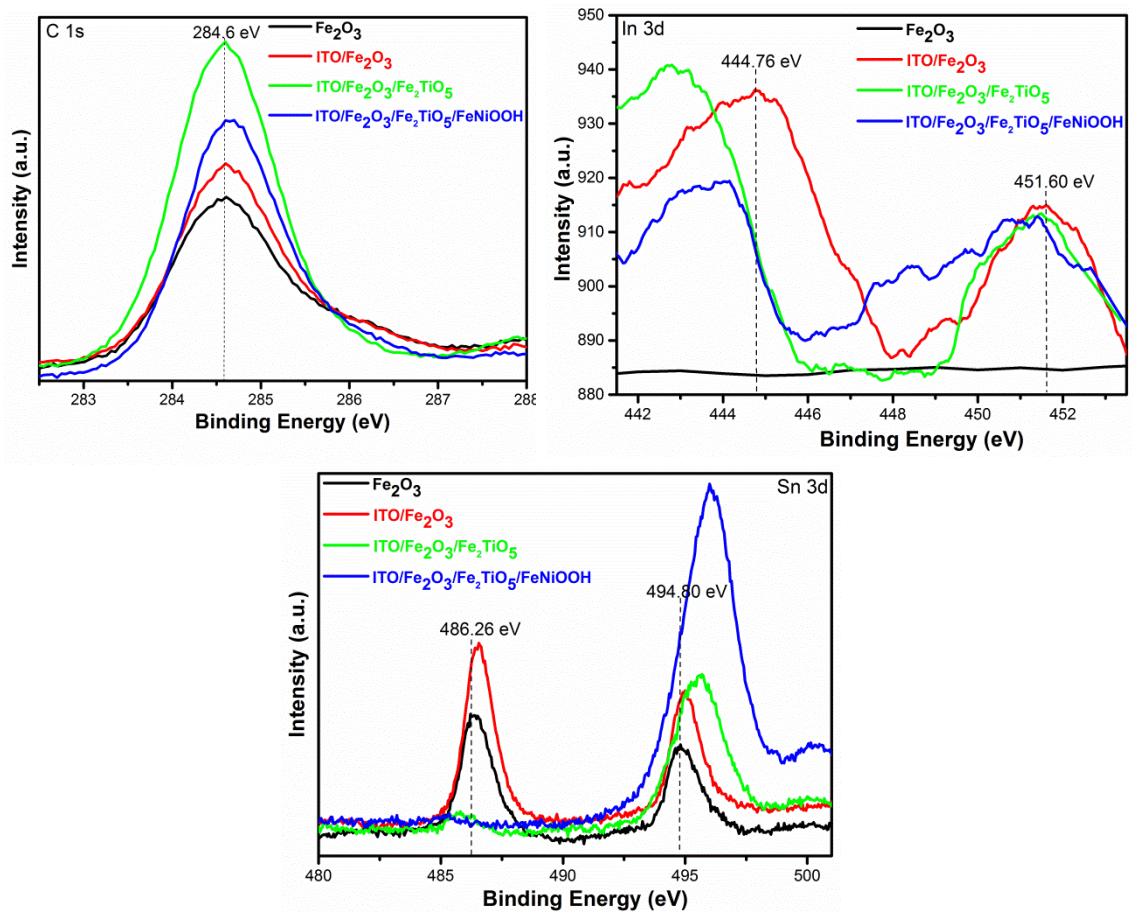


Figure S1. High resolution XPS spectra of C 1s, Sn 3d and In 3d of the Fe₂O₃, ITO/Fe₂O₃, ITO/Fe₂O₃/Fe₂TiO₅, and ITO/Fe₂O₃/Fe₂TiO₅/FeNiOOH electrodes.

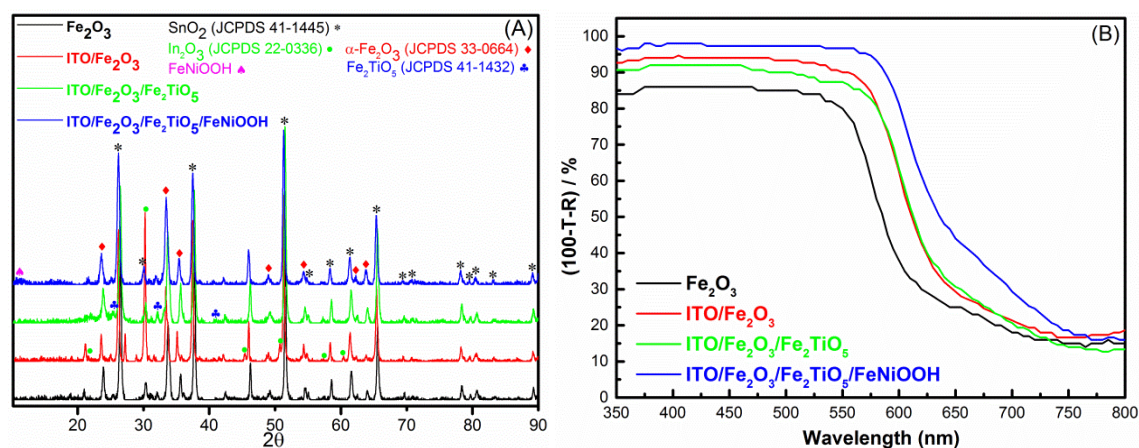


Figure S2. (A): Grazing incidence XRD patterns of the Fe_2O_3 , ITO/ Fe_2O_3 , ITO/ $\text{Fe}_2\text{O}_3/\text{Fe}_2\text{TiO}_5$, and ITO/ $\text{Fe}_2\text{O}_3/\text{Fe}_2\text{TiO}_5/\text{FeNiOOH}$ electrodes. (B): Absorbance of the Fe_2O_3 , ITO/ Fe_2O_3 , ITO/ $\text{Fe}_2\text{O}_3/\text{Fe}_2\text{TiO}_5$, and ITO/ $\text{Fe}_2\text{O}_3/\text{Fe}_2\text{TiO}_5/\text{FeNiOOH}$ electrodes; this plot was obtained from transmittance (T, %) and total reflectance (R, %) measurements on these electrodes by UV-Vis spectrum.

Characteristic XRD peaks of Fe_2O_3 (JCPDS no. 33-0664) and SnO_2 (JCPDS no. 41-1445, mainly derived from FTO substrate) can be observed in the four electrodes shown in Figure S2A. The XRD pattern of the ITO/ Fe_2O_3 , ITO/ $\text{Fe}_2\text{O}_3/\text{Fe}_2\text{TiO}_5$, and ITO/ $\text{Fe}_2\text{O}_3/\text{Fe}_2\text{TiO}_5/\text{FeNiOOH}$ electrodes exhibit the diffraction peaks assigned to In_2O_3 (JCPDS no. 22-0336) from the initial sputtered ITO underlayer. The diffraction peaks related to the pseudobrookite (Fe_2TiO_5 , JCPDS no. 41-1432) phase of ITO/ $\text{Fe}_2\text{O}_3/\text{Fe}_2\text{TiO}_5$, and ITO/ $\text{Fe}_2\text{O}_3/\text{Fe}_2\text{TiO}_5/\text{FeNiOOH}$ electrodes are very weak, which is attributed to the ultrathin shell (30 ALD cycles, estimated ca. 0.81 nm) of Fe_2TiO_5 coating.¹ Besides, there is a weak broad peak located at 11° , which can be assigned to the FeNiOOH ,²⁻⁴ indicating its poor crystalline structure. UV-vis absorbance spectra are obtained to account for the photo-activity of the Fe_2O_3 , ITO/ Fe_2O_3 , ITO/ $\text{Fe}_2\text{O}_3/\text{Fe}_2\text{TiO}_5$, and ITO/ $\text{Fe}_2\text{O}_3/\text{Fe}_2\text{TiO}_5/\text{FeNiOOH}$ electrodes, as shown in Figure S2B. All photoanodes exhibit an overall high absorption in the visible region (wavelength < 580 nm) with a relative steep absorption edge at approximately 580 nm.

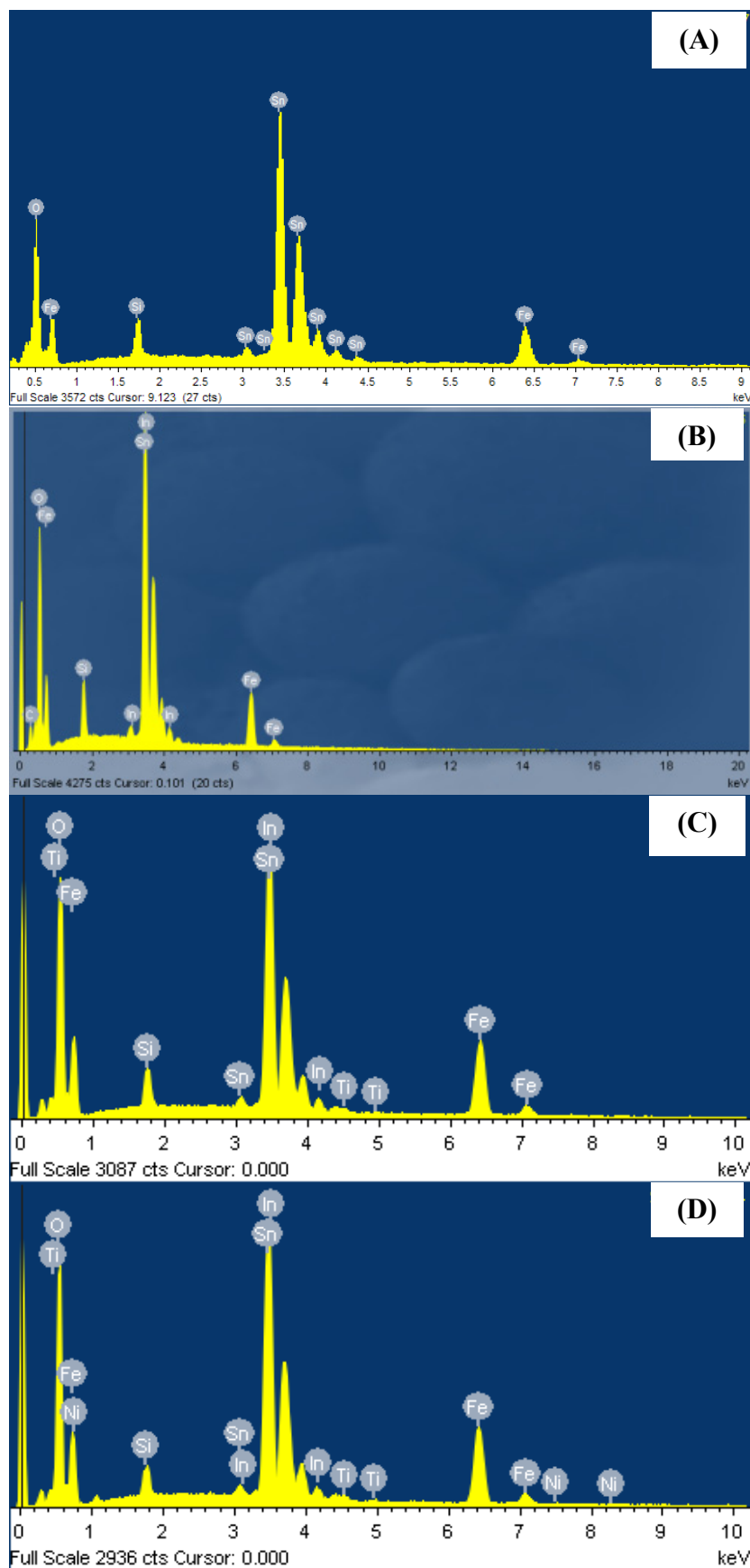


Figure S3. EDS obtained on the Fe_2O_3 (A), ITO/ Fe_2O_3 (B), ITO/ Fe_2O_3 / Fe_2TiO_5 (C), and ITO/ Fe_2O_3 / Fe_2TiO_5 /FeNiOOH (D) electrodes.

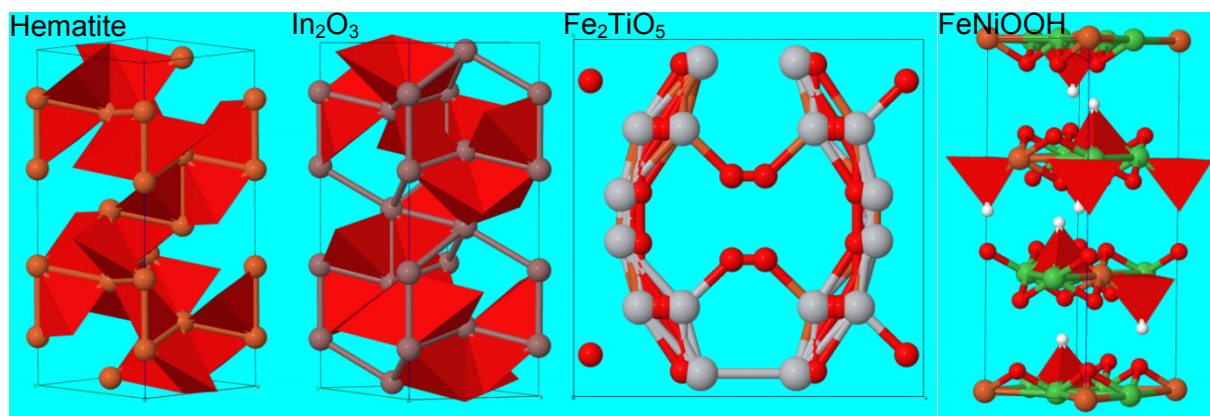


Figure S4. 1*1*1 unit crystal model of hematite, In₂O₃, Fe₂TiO₅ and FeNiOOH based on the crystal data in ICSD and reported data⁵ for the identification of the crystal phase.

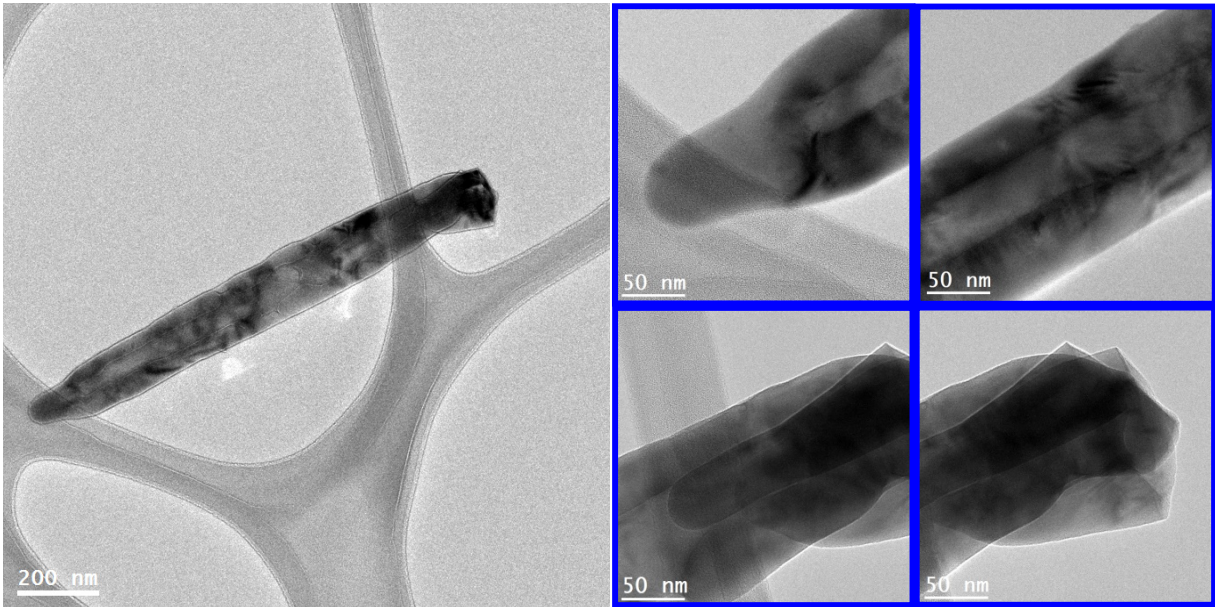


Figure S5. Low magnification TEM images of a nanowire from the Fe_2O_3 electrode. Left: low magnification TEM micrograph shows the nanowire morphology of the Fe_2O_3 electrode; Right: several TEM images showing the detailed structure of the Fe_2O_3 nanowire.

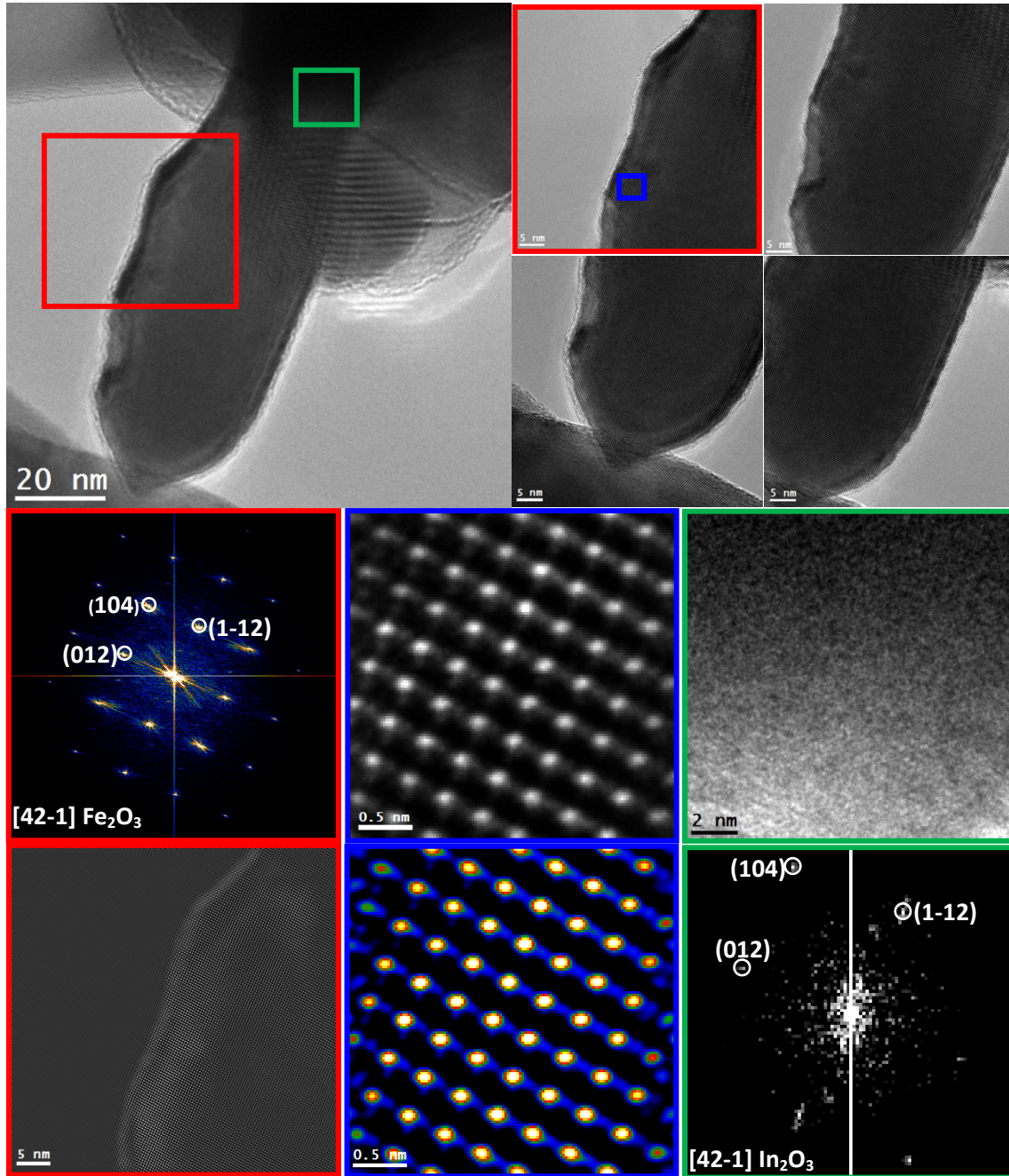


Figure S6. HRTEM, FFT spectrum and IFFT images obtained on a nanowire extracted from the ITO/Fe₂O₃ electrode.

Top rows: left: the low magnification TEM micrograph shows the morphology of a small Fe₂O₃ nanowire directly grown on ITO matrix; Right: the detailed crystal structure of different regions of the small nanowire.

Bottom rows: left column: the power spectrum of the red squared area indicating its single crystal structure corresponding to trigonal Fe₂O₃, [R3-CH]-Space group 167, also known as hematite, with lattice parameters of $a = b = 0.50342$ nm, $c = 1.37483$ nm, and $\alpha = \beta = 90^\circ$ and $\gamma = 120^\circ$ as visualized along the [42-1] direction; and the IFFT image of the red squared area. Middle column: the atomic HRTEM and temperature colored HRTEM of the blue squared area shows the ordered structure of hematite. Right column: the HRTEM of the green squared area and the corresponding reduced FFT spectrum indicates that the species can be assigned to Trigonal In₂O₃, [R3-CH]-space group 167, with lattice parameters of $a = b = 0.5438$ nm, $c = 1.4474$ nm, and $\alpha = \beta = 90^\circ$ and $\gamma = 120^\circ$ as visualized along [42-1] direction.

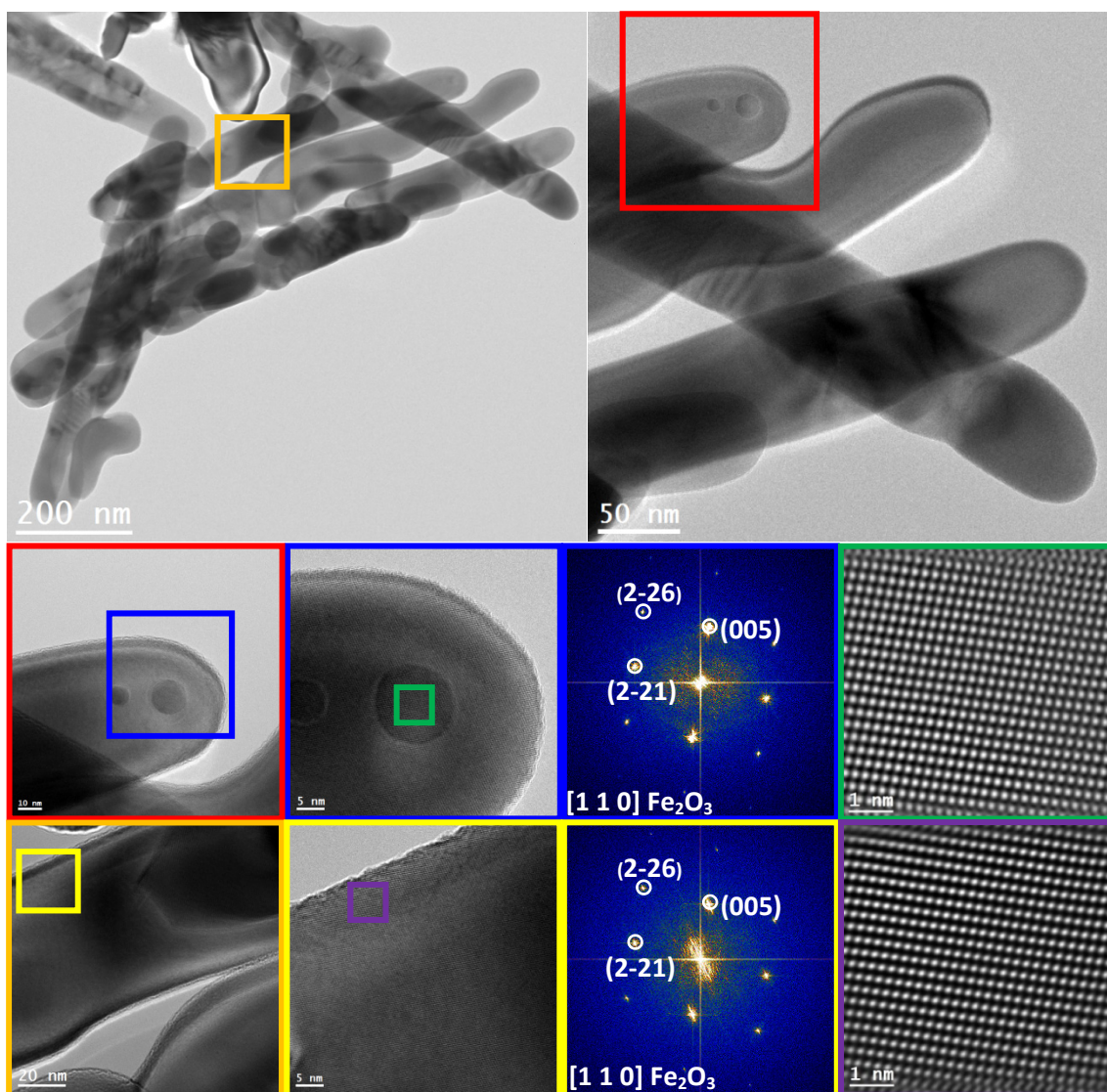


Figure S7. HRTEM, FFT spectrum and IFFT images corresponding to nanowire-like structures extracted from the ITO/Fe₂O₃ electrode. Top rows: left: low magnification TEM micrograph shows the distribution of several nanowires; Right: the magnified TEM images of these nanowires. Middle rows: left: HRTEM obtained on the red squared area; Middle: the detailed structure obtained on the blue squared area and its corresponding power spectrum indicating its hematite single crystal structure as visualized along the [110] direction; Right: atomic IFFT image of the green squared area. Bottom rows: left: HRTEM micrograph corresponding to the orange squared area; Middle: detail structure in the yellow squared area and the corresponding power spectrum indicating its hematite single crystal structure as visualized along the [110] direction; Right: atomic IFFT image of the purple squared area.

As can be seen from Figure S6, Trigonal In₂O₃ phase is identified at the bulk matrix, where the small Fe₂O₃ nanowires are directly grown onto. It is noteworthy that the Fe₂O₃ nanowires grown with a ITO under layer presents single crystal hematite phase, as confirmed by the FFT spectrum and atomic resolution HRTEM displayed in Figures S6 and S7. The improved crystal quality of Fe₂O₃ nanowires may be derived from the epitaxial relationship between Fe₂O₃ and In₂O₃ phase since they belong to the same Space group-167 [R3-CH] and with similar crystal constant. Besides, Figure S7 indicates that even the nanowire structure shows a slightly curved-shape, the nanowires crystal orientation does not vary at different regions.

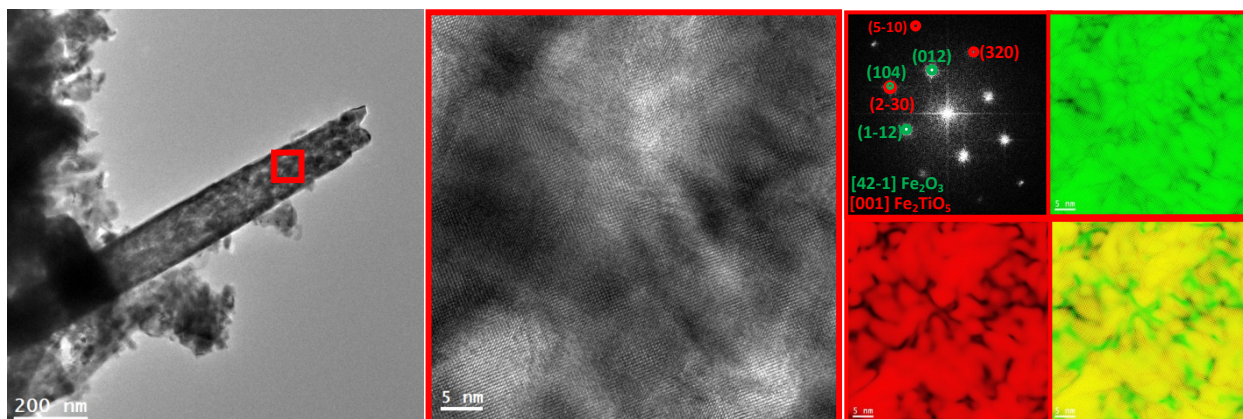


Figure S8. HRTEM and RGB IFFT images of ITO/Fe₂O₃/Fe₂TiO₅ electrode. left: low magnification TEM image showing a Fe₂O₃/Fe₂TiO₅ composite nanowire directly grown on the ITO matrix; Middle: detail of structure at the red squared area; Right: the corresponding power spectrum indicating it is composed of hematite and pseudobrookite visualized along [42-1] and [001] directions, respectively; and the RGB IFFT images of hematite, pseudobrookite and their composite, indicating the homogeneously coating of pseudobrookite on the surface of the hematite nanowires.

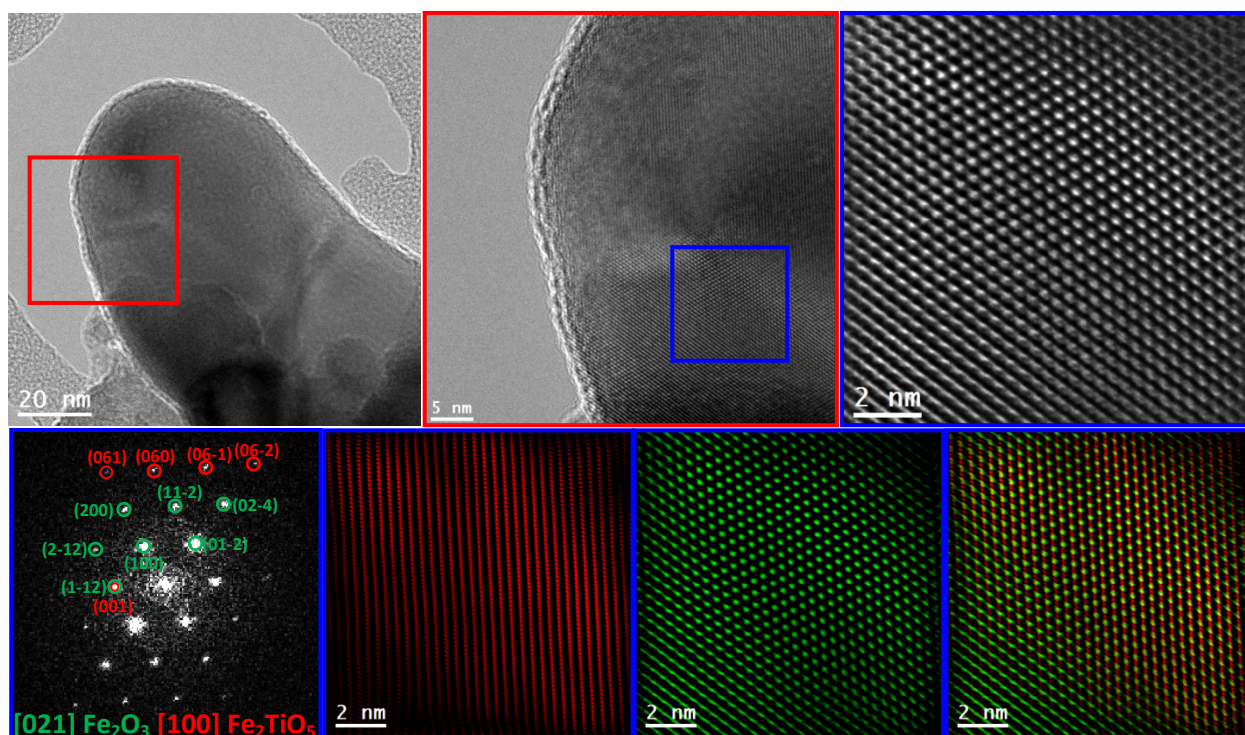


Figure S9. HRTEM and RGB IFFT images in the nanowires-like structure extracted from the ITO/Fe₂O₃/Fe₂TiO₅ electrode.

Top row: Left: low magnification TEM micrograph showing the edge of the nanowire; Middle: HRTEM detail corresponding to the red squared region; Right: detail of the structure in the blue rectangle region.

Bottom row: Left: the corresponding power spectrum of blue squared region indicating it is composed of hematite and pseudobrookite visualized along [021] and [100] directions, respectively; and the RGB IFFT images of hematite (green), pseudobrookite (red) and their composite, showing the atomic stack sequence of hematite and pseudobrookite.

As we can see from Figures S8 and S9, the low magnification IFFT RGB and the atomic IFFT RGB images together demonstrate the homogeneously coating of Fe₂TiO₅ onto Fe₂O₃ nanowires in the case of ITO/Fe₂O₃/Fe₂TiO₅ electrode.

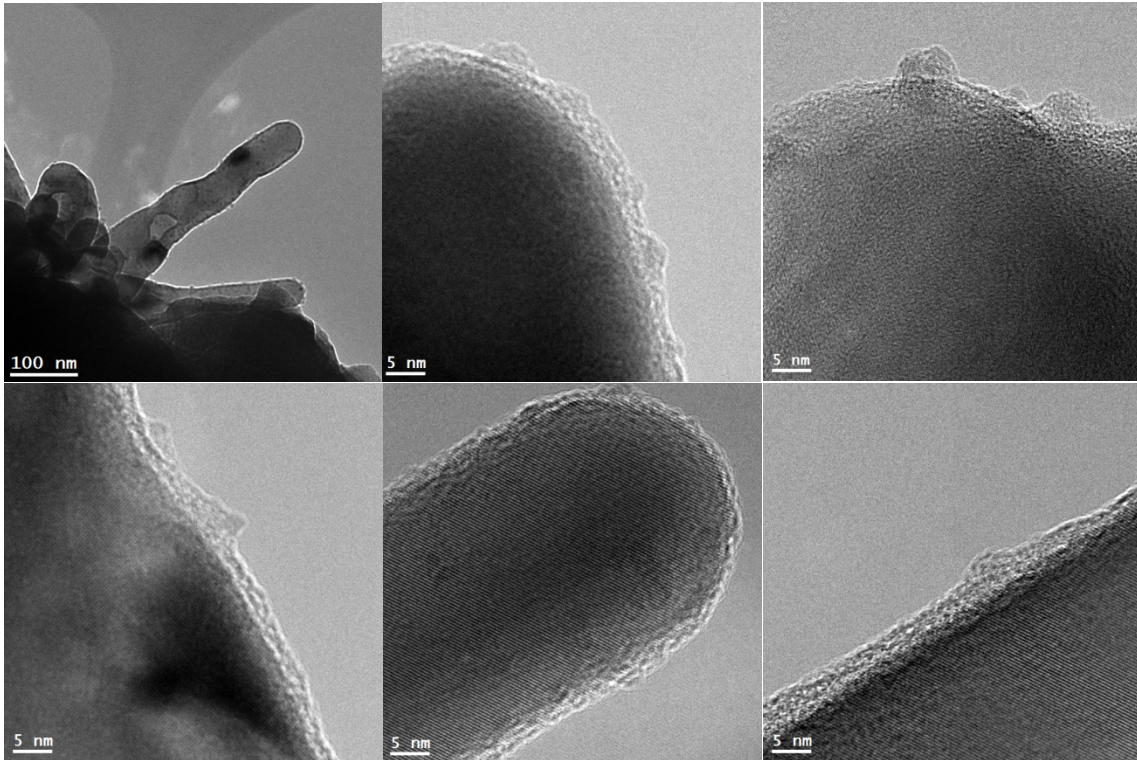


Figure S10. Several TEM images showing the distribution of FeNiOOH nanodots on the surface of $\text{Fe}_2\text{O}_3/\text{Fe}_2\text{TiO}_5$ composite nanowires of ITO/ $\text{Fe}_2\text{O}_3/\text{Fe}_2\text{TiO}_5/\text{FeNiOOH}$ electrode.

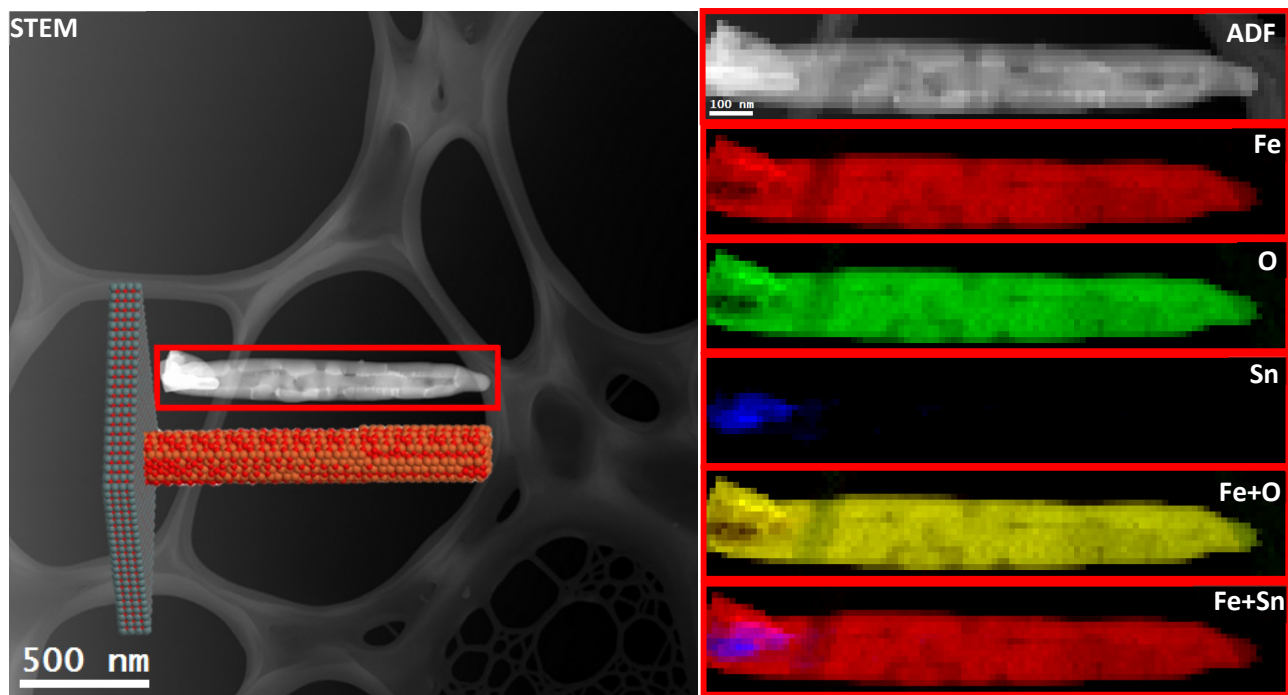


Figure S11. EELS chemical composition maps obtained from the red rectangled area of the ADF-STEM micrograph of a nanowire extracted from the Fe_2O_3 electrode. Individual Fe (red), O (green), Sn (blue) maps and their composite. (The inset of the ADF-STEM micrograph shows the atomic model for Fe_2O_3 electrode)

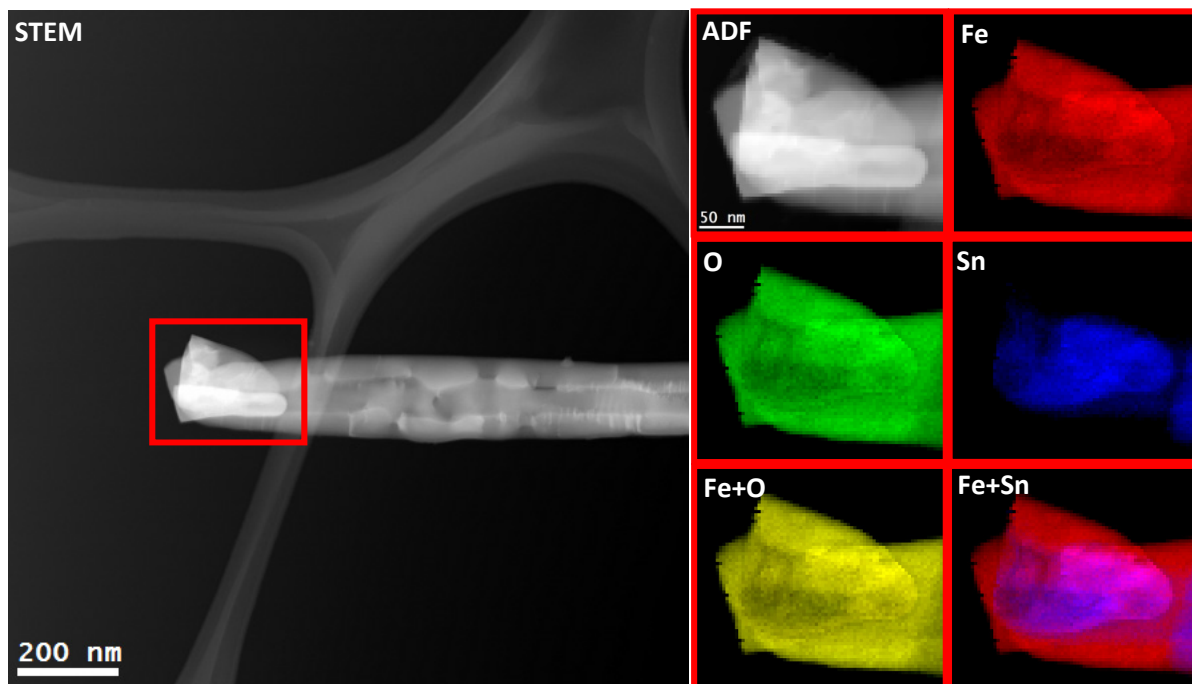


Figure S12. EELS chemical composition maps obtained from the red rectangled area of the ADF-STEM micrograph of a nanowire extracted from the Fe_2O_3 electrode. Individual Fe (red), O (green), Sn (blue) maps and their composite.

As displayed in Figures S11 and S12, the diameter and length of the Fe_2O_3 nanowires from the Fe_2O_3 electrode are estimated to be ca. 50 nm and 1 μm , respectively. The STEM-EELS mappings (Figures S11 and S12) reveal that the Sn elemental signal is only present at the bottom part of the Fe_2O_3 nanowire, the diameter of which is bigger than the top region of the nanowire. The Sn diffusion in the case of the Fe_2O_3 electrode is much weaker than that in the ITO/ Fe_2O_3 , ITO/ Fe_2O_3 / Fe_2TiO_5 , and ITO/ Fe_2O_3 / Fe_2TiO_5 / FeNiOOH electrodes, respectively, as we will see below in Figures S13- S17.

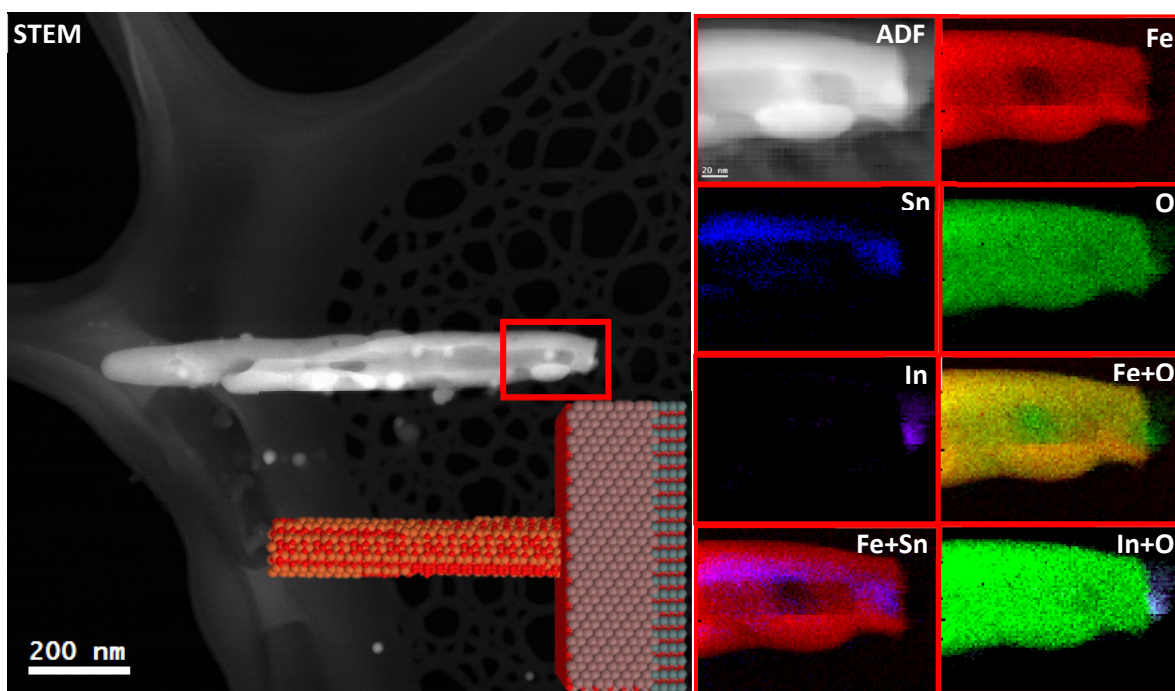


Figure S13. EELS chemical composition maps obtained from the red rectangled area of the ADF-STEM micrograph in the nanowire-like structure extracted from the ITO/Fe₂O₃ electrode. Individual Fe (red), O (green), Sn (blue) and In (purple) maps and their composite. (The inset of the ADF-STEM micrograph shows the atomic model for ITO/Fe₂O₃ electrode).

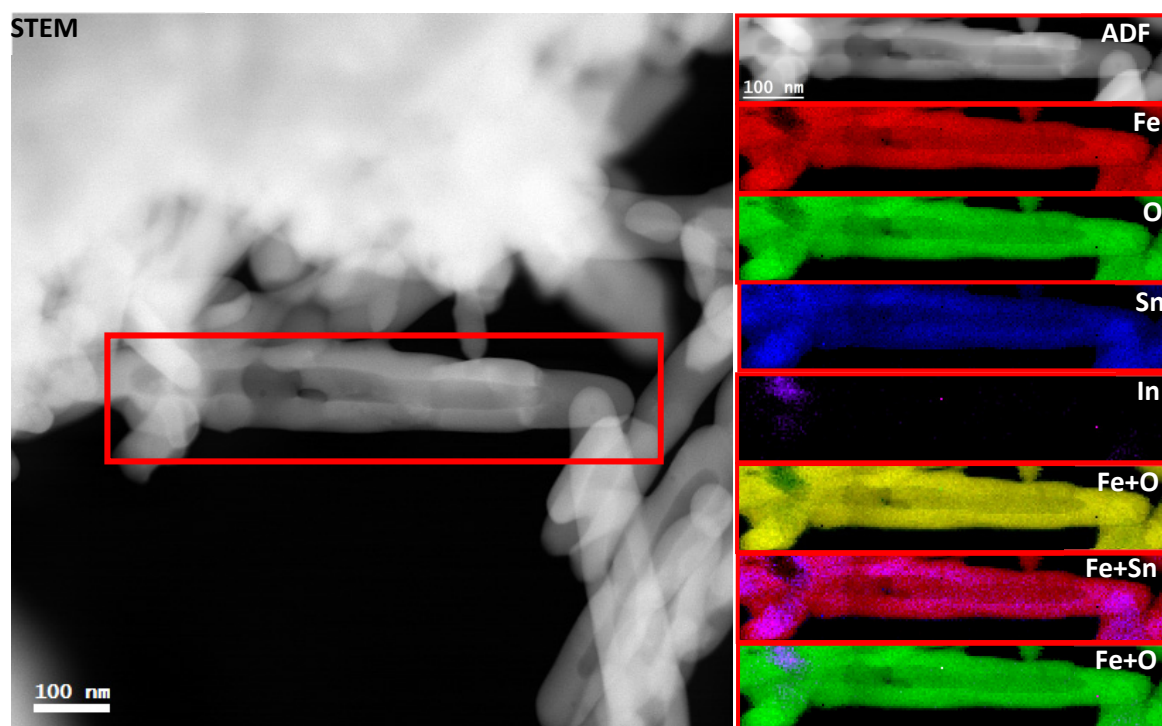


Figure S14. EELS chemical composition maps obtained from the red rectangled area of the ADF-STEM micrograph in the nanowire-like structure extracted from ITO/Fe₂O₃ electrode. Individual Fe (red), O (green), Sn (blue) and In (purple) maps and their composite.

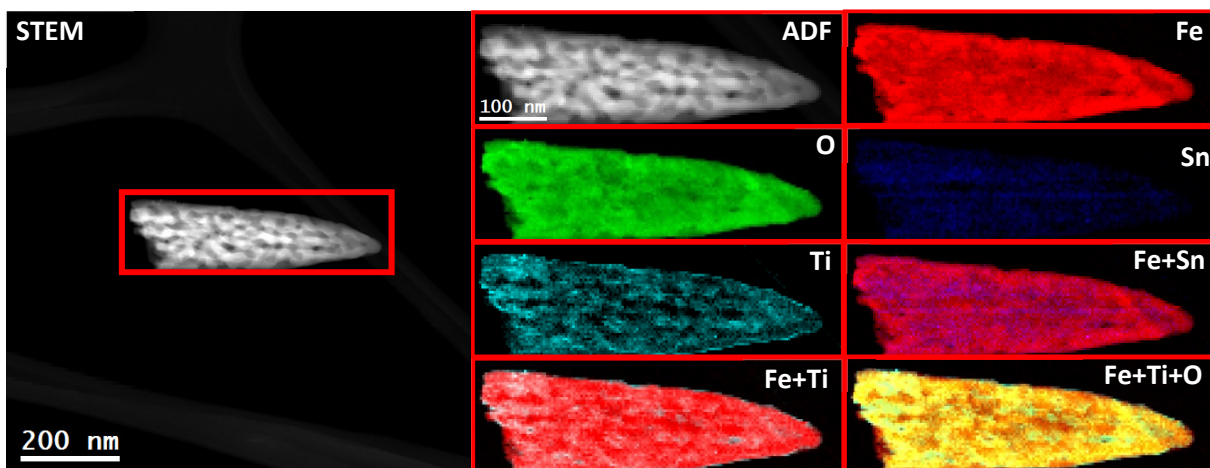


Figure S15. EELS chemical composition maps obtained from the red rectangled area of the ADF-STEM micrograph in the nanowire-like structure extracted from ITO/Fe₂O₃/Fe₂TiO₅ electrode. Individual Fe (red), O (green), Sn (blue) and Ti (indigo) maps and their composite.

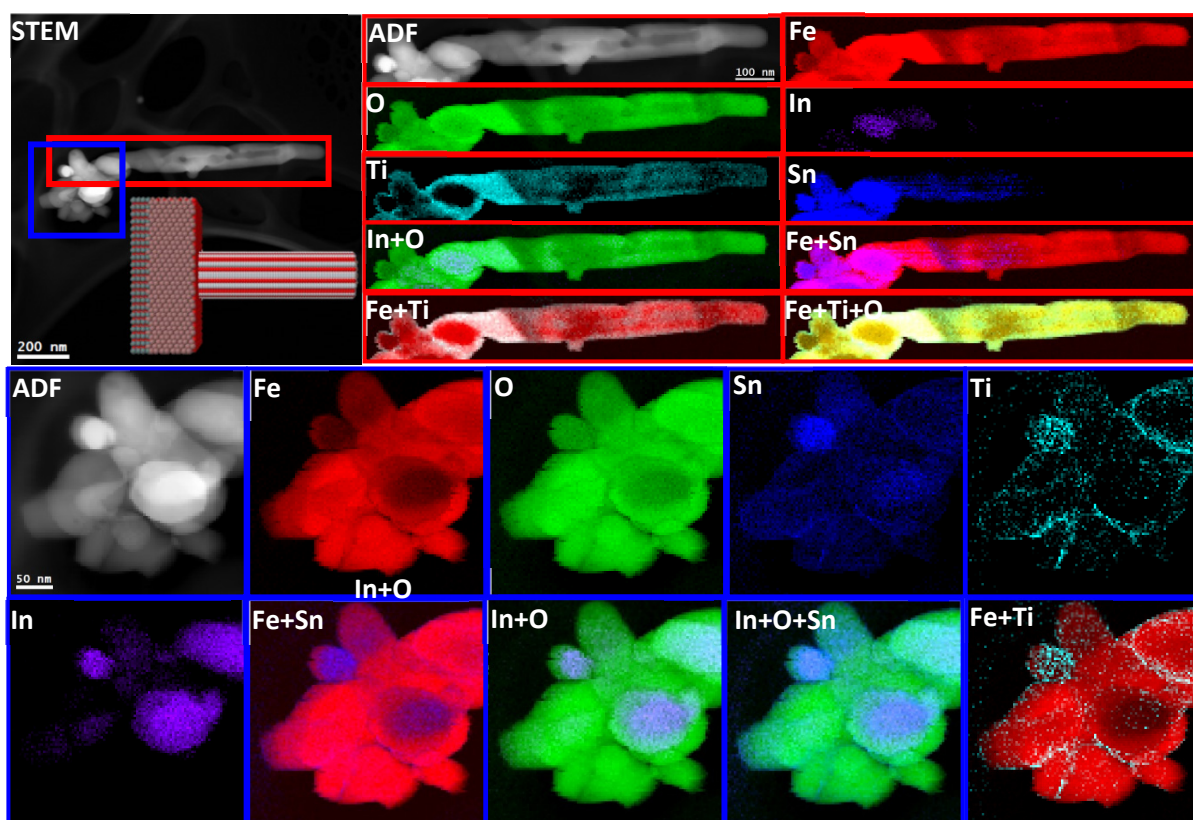


Figure S16. EELS chemical composition maps obtained from the red and blue rectangled area of the ADF-STEM micrograph in the nanowire-like structure extracted from ITO/Fe₂O₃/Fe₂TiO₅ electrode. Individual Fe (red), O (green), Sn (blue), In (purple) and Ti (indigo) maps and their composite. (The inset of the ADF-STEM micrograph shows the atomic model for ITO/Fe₂O₃/Fe₂TiO₅ electrode).

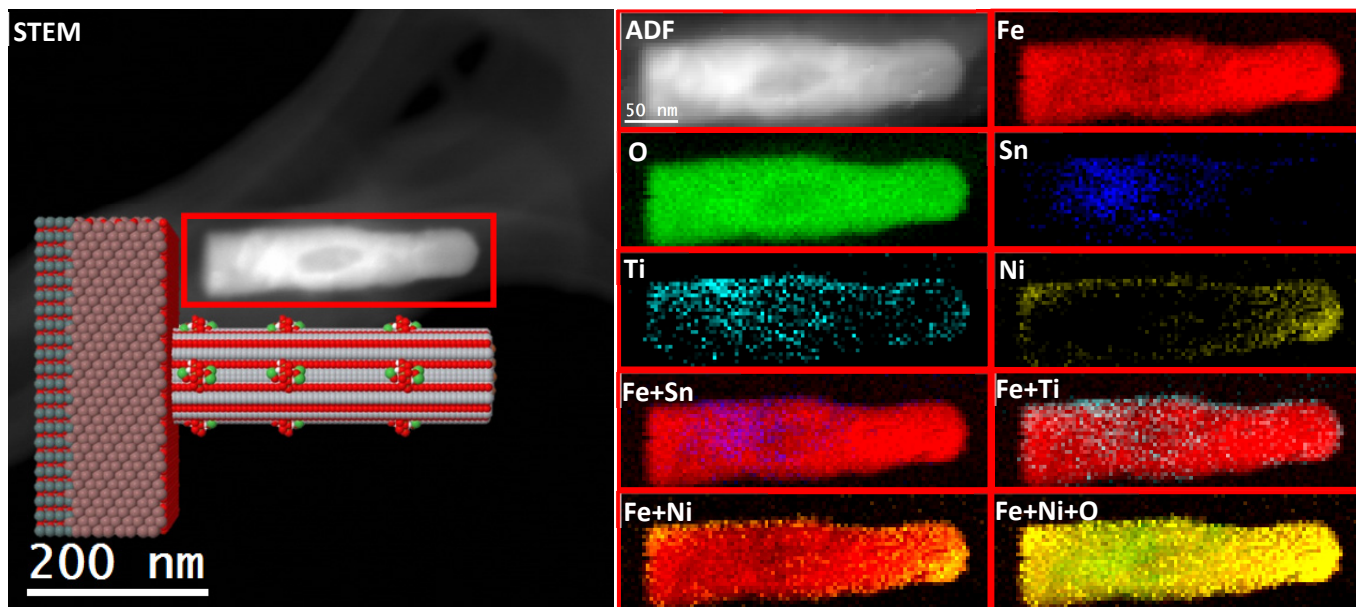


Figure S17. EELS chemical composition maps obtained from the red rectangled area of the ADF-STEM micrograph in the nanowire-like structure extracted from ITO/Fe₂O₃/Fe₂TiO₅/FeNiOOH electrode. Individual Fe (red), O (green), Sn (blue), Ti (indigo) and Ni (yellow) maps and their composite. (The inset of the ADF-STEM micrograph shows the atomic model for ITO/Fe₂O₃/Fe₂TiO₅/FeNiOOH electrode).

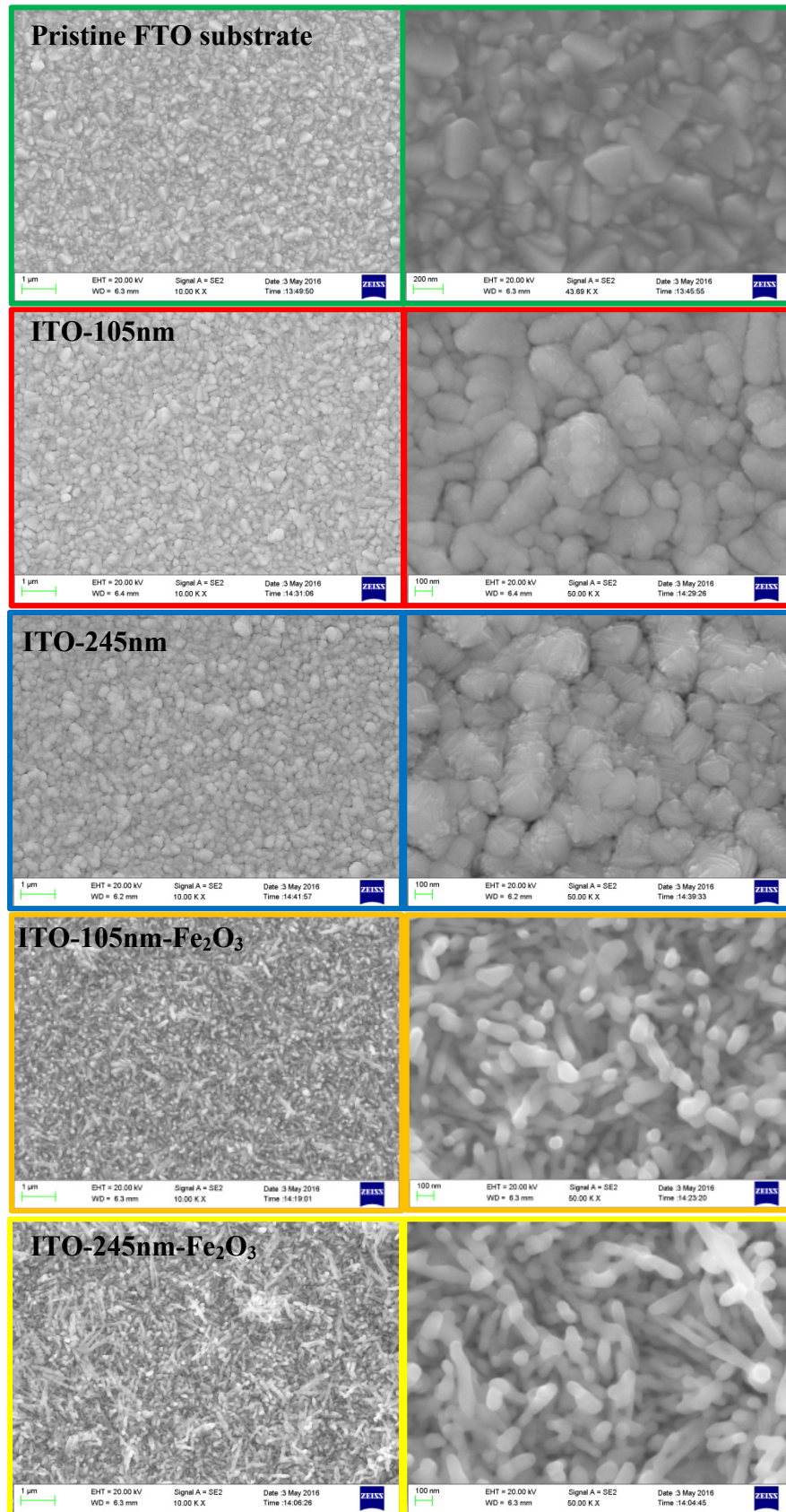


Figure S18. SEM images of the pristine FTO substrate, ITO-105 nm, ITO-245 nm, ITO-105 nm-Fe₂O₃ and ITO-245 nm-Fe₂O₃ electrodes.

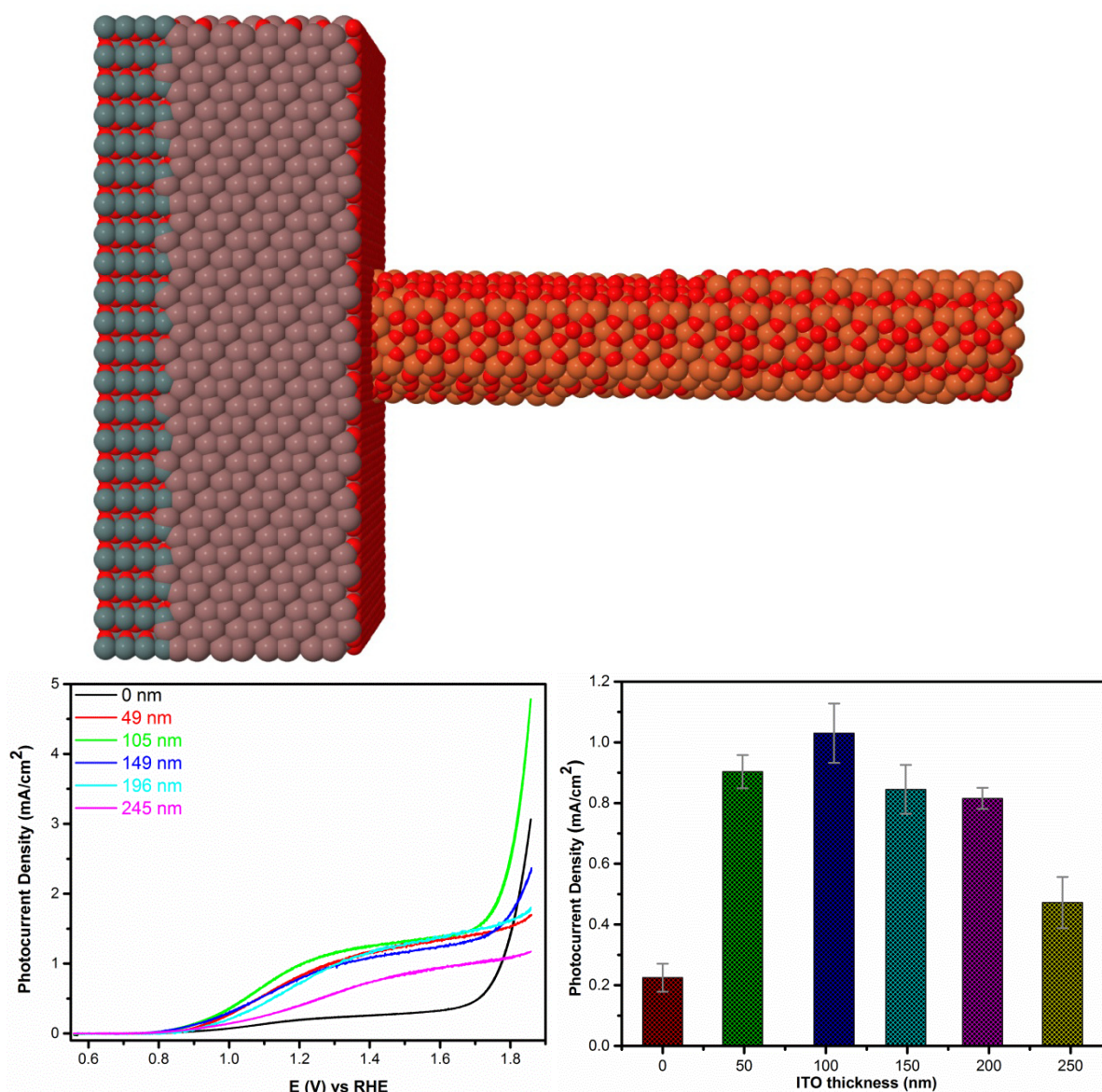


Figure S19. Top: the atomic model for optimized ITO/Fe₂O₃ electrodes. Bottom: Left: CV curves of the ITO/Fe₂O₃ electrodes with different ITO thickness sintering on 750 °C for 30min under illumination; Right: the photocurrent density at 1.23 V vs. RHE related to the ITO thickness (the error bar stemmed from the standard deviation of statistic data collected at least three repeated electrodes).

As displayed in Figure S19, with the increment of ITO deposition thickness from 0 nm to 105 nm, the photocurrent at 1.23 V vs. RHE gradually increases to 1.05 mA cm⁻². In stark contrast, the corresponding photocurrent at 1.23 V vs. RHE decreases intensively upon further extending ITO deposition thickness to 245 nm. This intensive reduction of photocurrent might be attributed to the deteriorated nanowire structure of hematite because of the exorbitantly doped Sn from the thick ITO matrix, which is evidenced by the randomly inclined hematite nanowires of ITO-245nm-Fe₂O₃ electrode as shown in Figure S18.

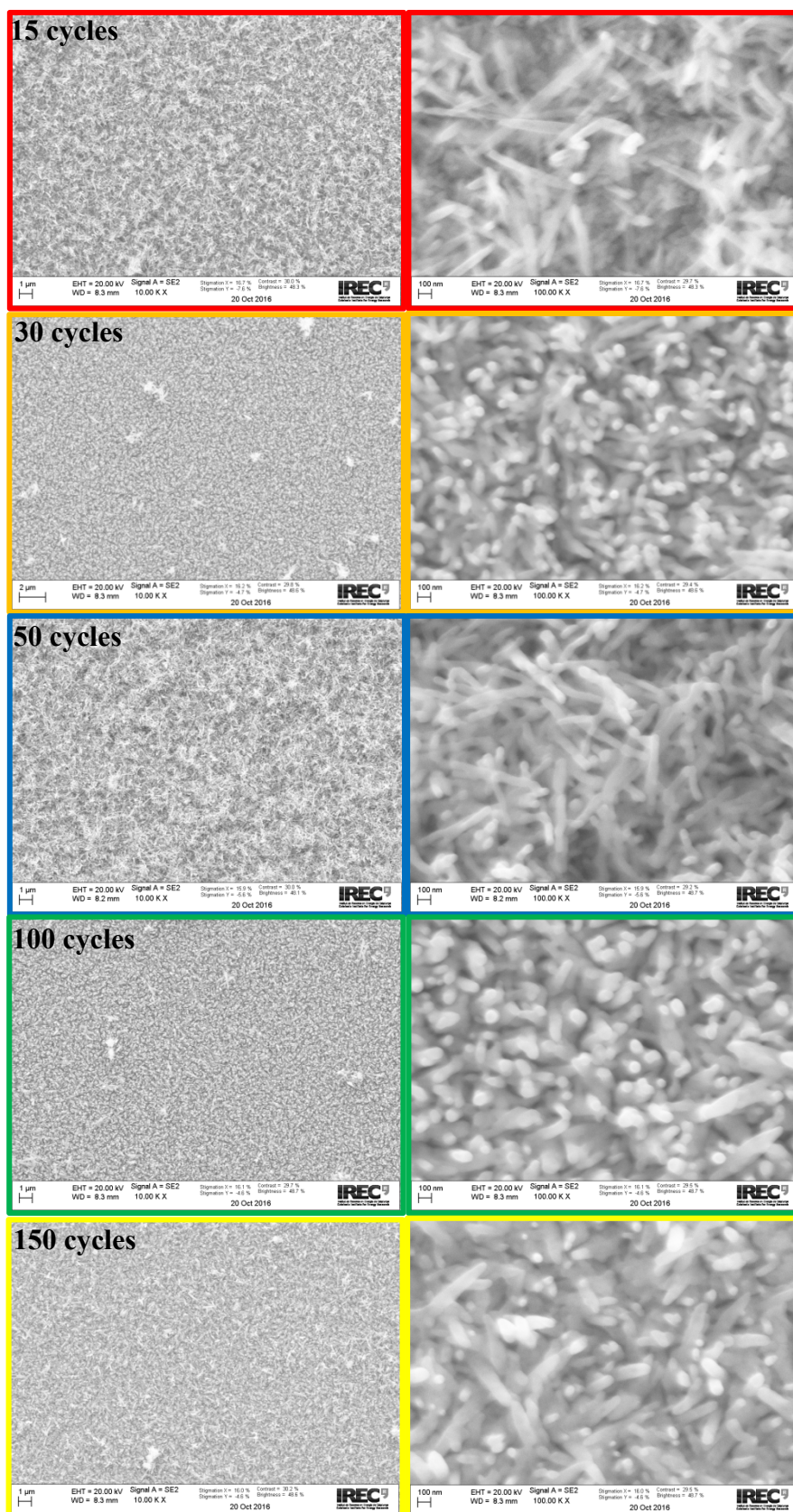


Figure S20. SEM images of the ITO/Fe₂O₃/Fe₂TiO₅ electrodes with different ALD cycles (TiO₂ thickness), e.g. 15 cycles, 30 cycles, 50 cycles, 100 cycles and 150 cycles.

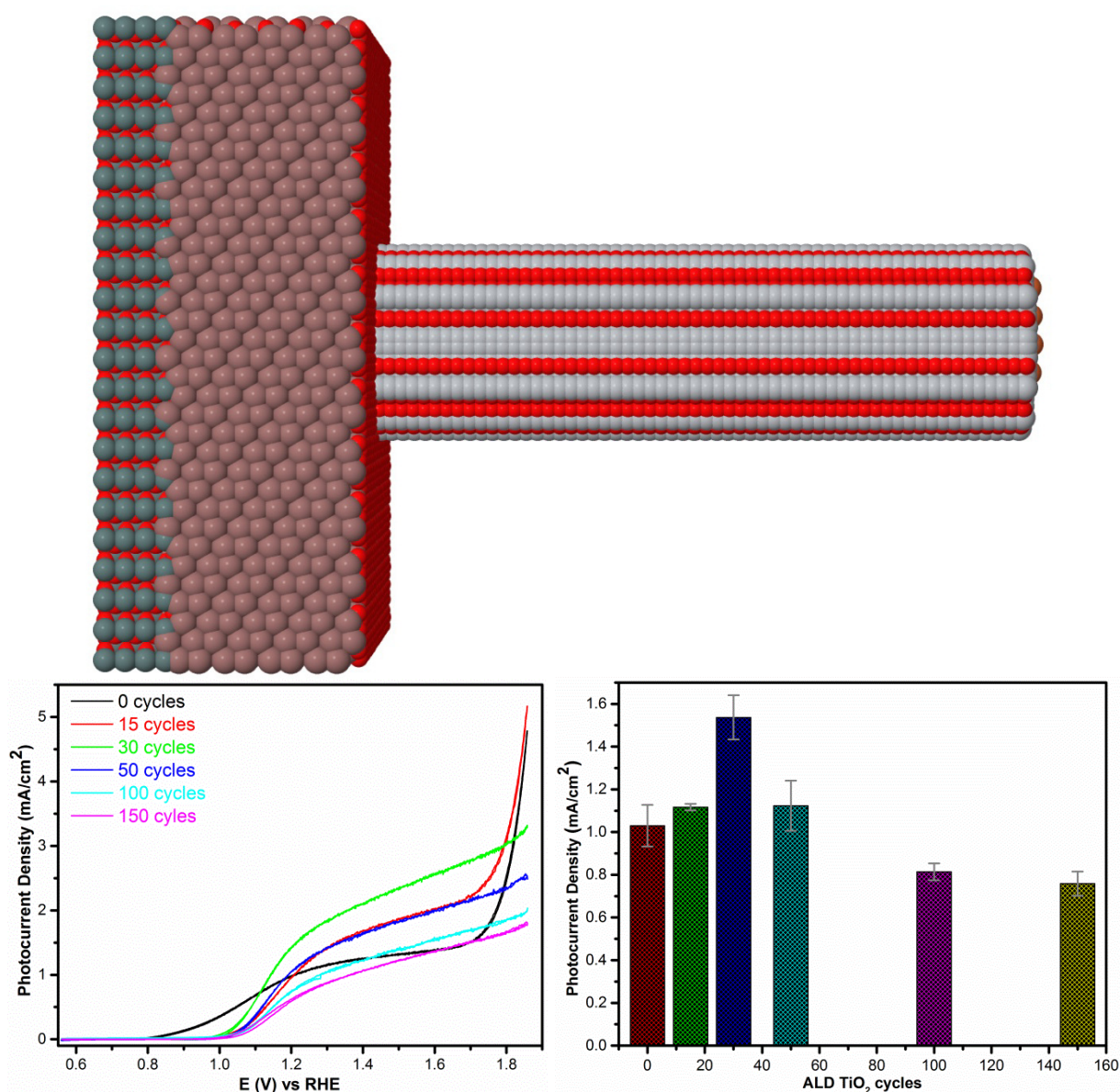


Figure S21. Top: the atomic model for optimized ITO/Fe₂O₃/Fe₂TiO₅ electrodes. Bottom: Left: CV curves of the ITO/Fe₂O₃/Fe₂TiO₅ electrodes with different ALD TiO₂ cycles (thickness) sintering on 750 °C for 30 min under illumination; Right: the photocurrent density at 1.23 V vs. RHE related to the ALD TiO₂ cycles (the error bar stemmed from the standard deviation of statistic data collected at least three repeated electrodes).

Figures S20 and S21 correlate the photocurrent response of the ITO/Fe₂O₃/Fe₂TiO₅ electrodes with the ALD TiO₂ deposition cycles. Figure S21 exhibits the photocurrent of the ITO/Fe₂O₃/Fe₂TiO₅ electrodes varies with the increment of ALD TiO₂ deposition cycles. At 30 ALD TiO₂ deposition cycles, the ITO/Fe₂O₃/Fe₂TiO₅ electrode possess the highest photocurrent of 1.56 mA cm⁻², indicating suitable coating of the Fe₂TiO₅ onto the ITO/Fe₂O₃ electrode, without residual TiO₂ on the surface of the ITO/Fe₂O₃/Fe₂TiO₅ electrode and the formation of deleterious heterojunction like the Fe₂O₃/Fe₂TiO₅/TiO₂,⁶ as confirmed by Figures S8-S9 and S15–S16.

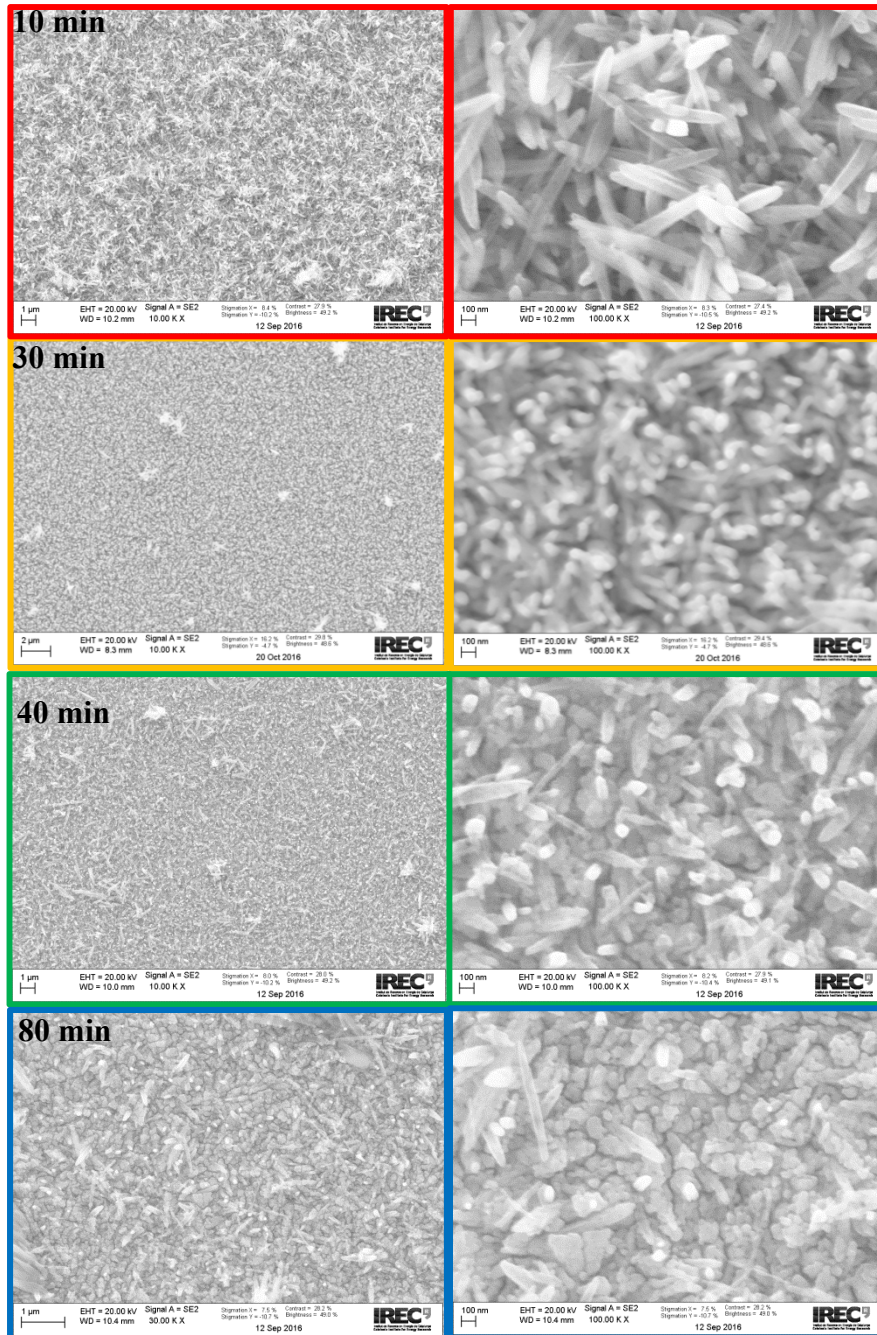


Figure S22. SEM images of the ITO/Fe₂O₃/Fe₂TiO₅-30 cycles electrodes with different sintering time at 750°C, e.g. 10 min, 30 min, 40 min and 80 min.

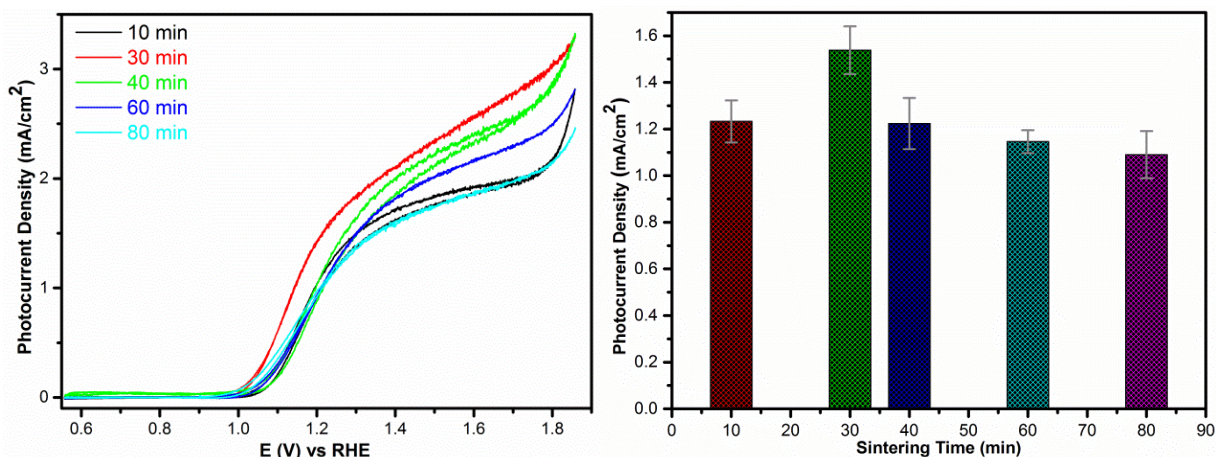
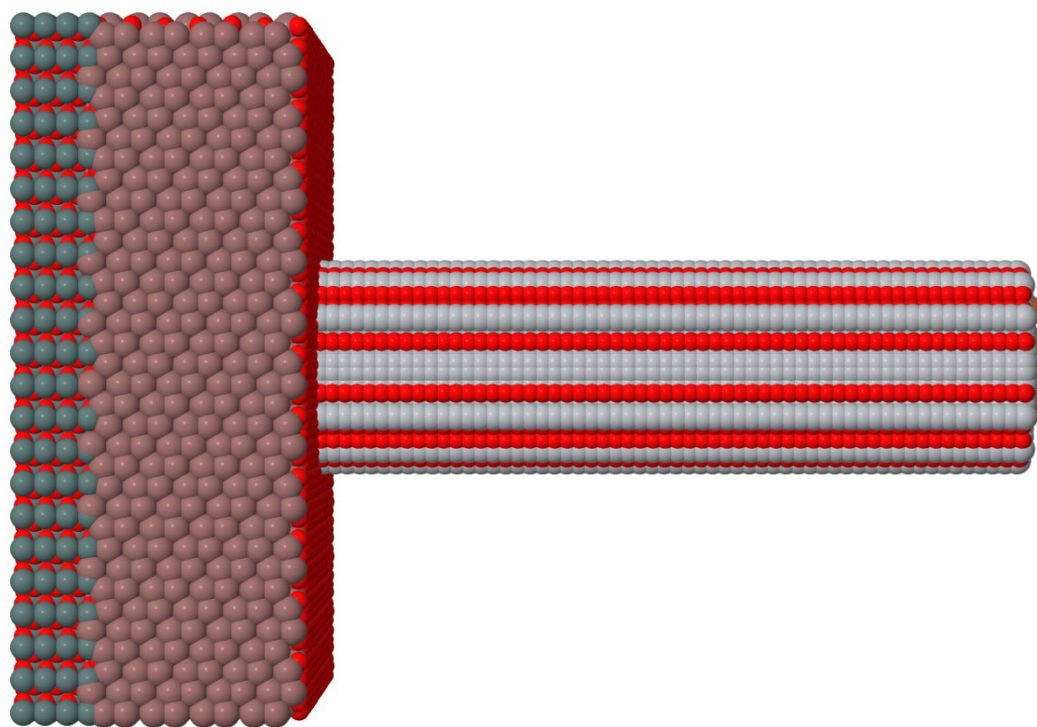


Figure S23. Top: the atomic model for optimized ITO/Fe₂O₃/Fe₂TiO₅ electrodes. Bottom: Left: CV curves of the ITO/Fe₂O₃/Fe₂TiO₅-30 cycles electrodes with different sintering time on 750 °C under illumination; Right: the photocurrent density at 1.23 V vs. RHE related to the sintering time (the error bar stemmed from the standard deviation of statistic data collected at least three repeated electrodes).

In order to reduce the surface defects, enhance the Sn doping and retain the nanostructure texturing of hematite nanowires at the same time, an optimization of sintering time for the ITO/Fe₂O₃/Fe₂TiO₅-30 cycles electrode has been performed, as shown in Figures S22 and S23. Figure S22 reveals the sintering time substantially affect the morphology of the Fe₂O₃/Fe₂TiO₅ nanowires. As the sintering time over 30 min at 750 °C, the Fe₂O₃/Fe₂TiO₅ nanowires initiate the deformation and finally evolve into a film-like structure, which somehow reduce the surface area exposure to electrolyte. The monitoring of the PEC performance in Figure S23 indicates the highest photocurrent response of the ITO/Fe₂O₃/Fe₂TiO₅-30 cycles electrode can be obtained with sintering parameter at 750 °C for 30min.

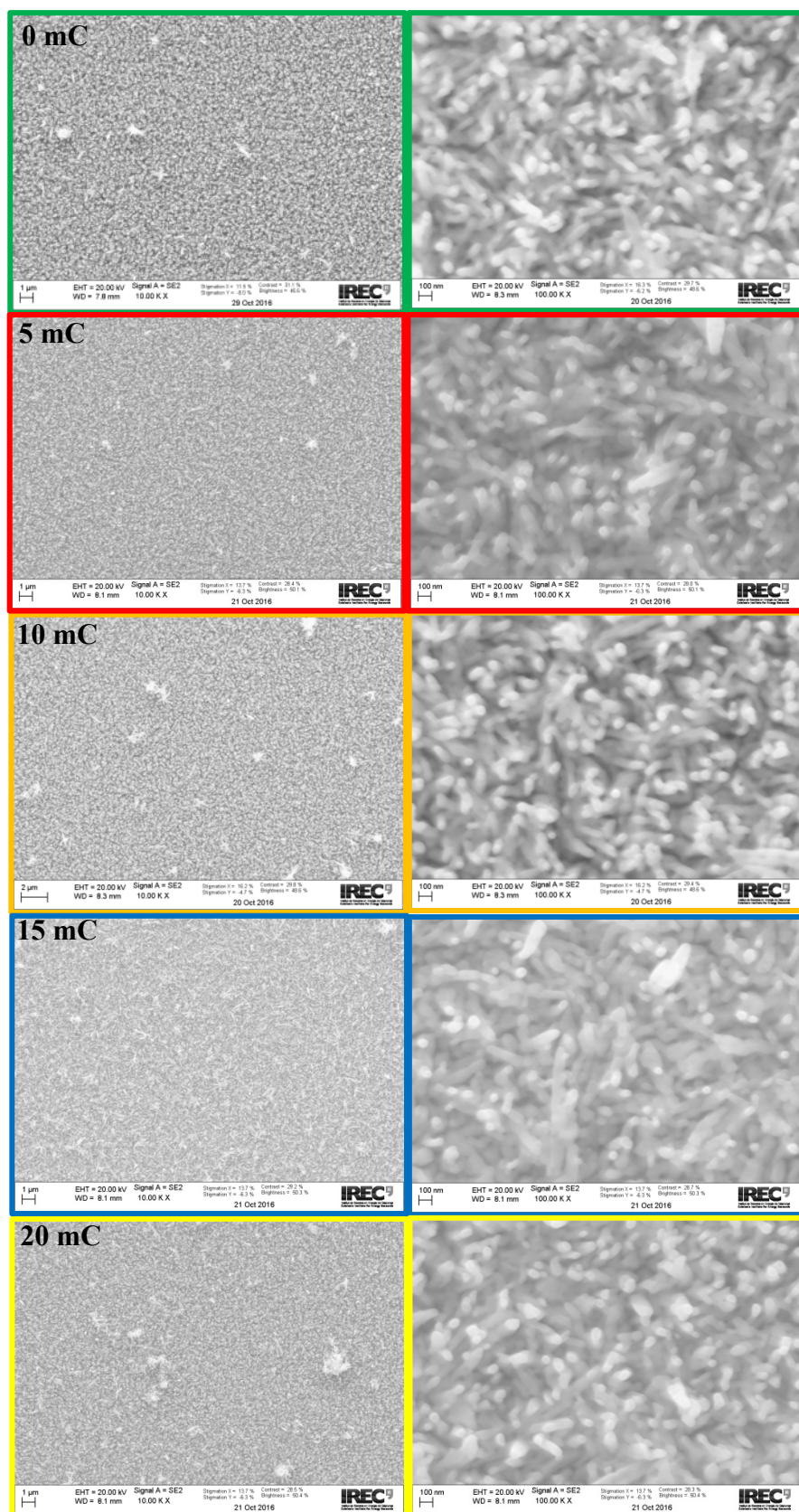


Figure S24. SEM images of the ITO/Fe₂O₃/Fe₂TiO₅/FeNiOOH electrodes with different FeNiOOH deposition charge, e.g. 0 mC, 5 mC, 10 mC, 15 mC and 20 mC.

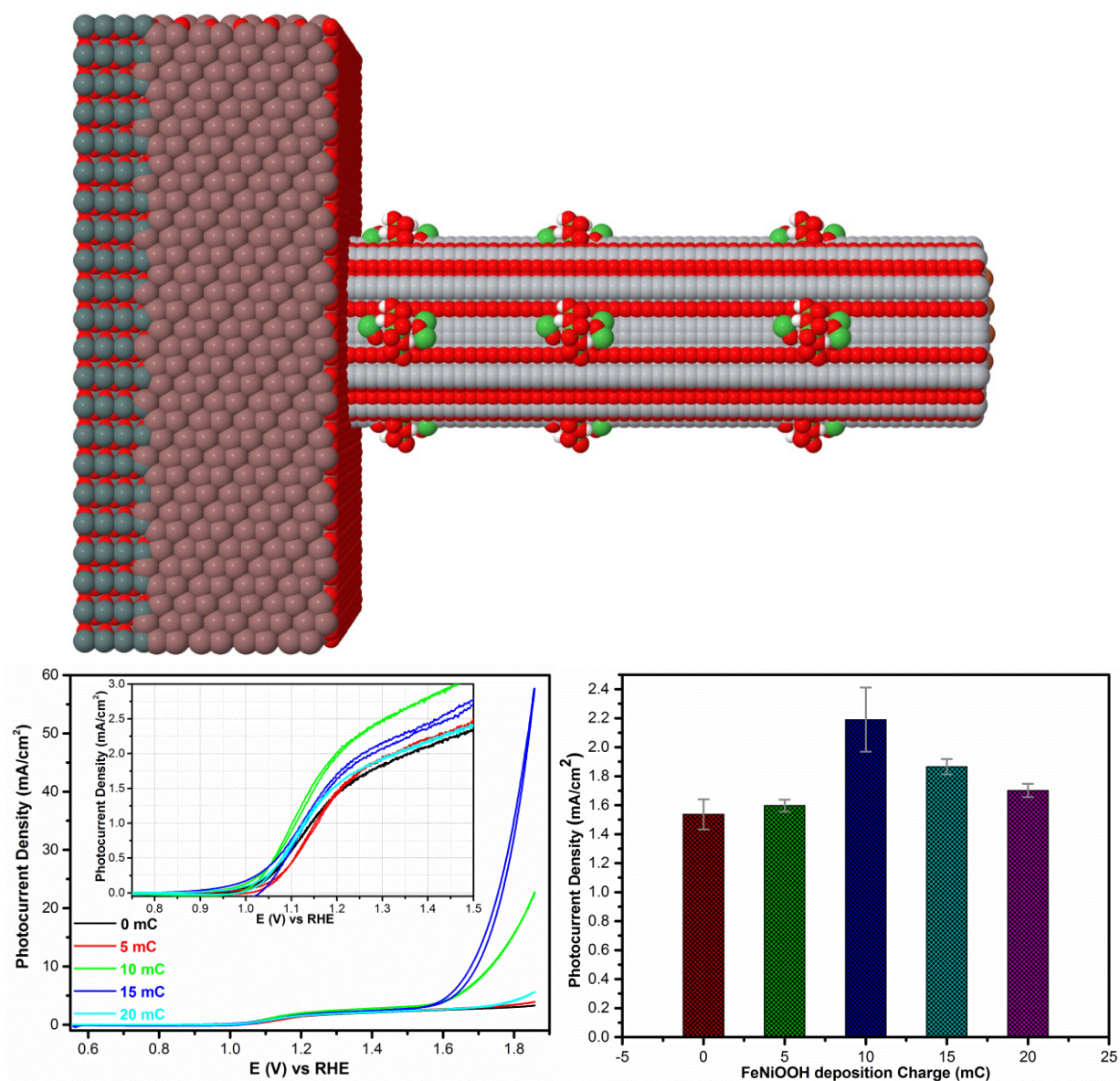


Figure S25. Top: the atomic model for the optimized ITO/Fe₂O₃/Fe₂TiO₅/FeNiOOH electrode. Bottom: Left: CV curves of the ITO/Fe₂O₃/Fe₂TiO₅/FeNiOOH electrodes with different FeNiOOH deposition charge under illumination; Right: the photocurrent density at 1.23 V vs. RHE related to the FeNiOOH deposition charge (the error bar stemmed from the standard deviation of statistic data collected at least three repeated electrodes).

It is well established that the OER activity of the FeNiOOH can be adjusted according to the OEC film thickness.⁷⁻⁹ In our case, the electrodeposition charges of FeNiOOH onto ITO/Fe₂O₃/Fe₂TiO₅ electrode have been optimized, as displayed in Figures S24 and S25. With the 10 mC decorations of the FeNiOOH nanodots, the photocurrent of the ITO/Fe₂O₃/Fe₂TiO₅ electrode can be further enhanced to 2.2 mA cm⁻². It reveals that coupling the FeNiOOH on the ITO/Fe₂O₃/Fe₂TiO₅ electrode effectively suppress the electron-hole pair recombination and accelerate reaction kinetics at the SEI.¹⁰⁻¹¹

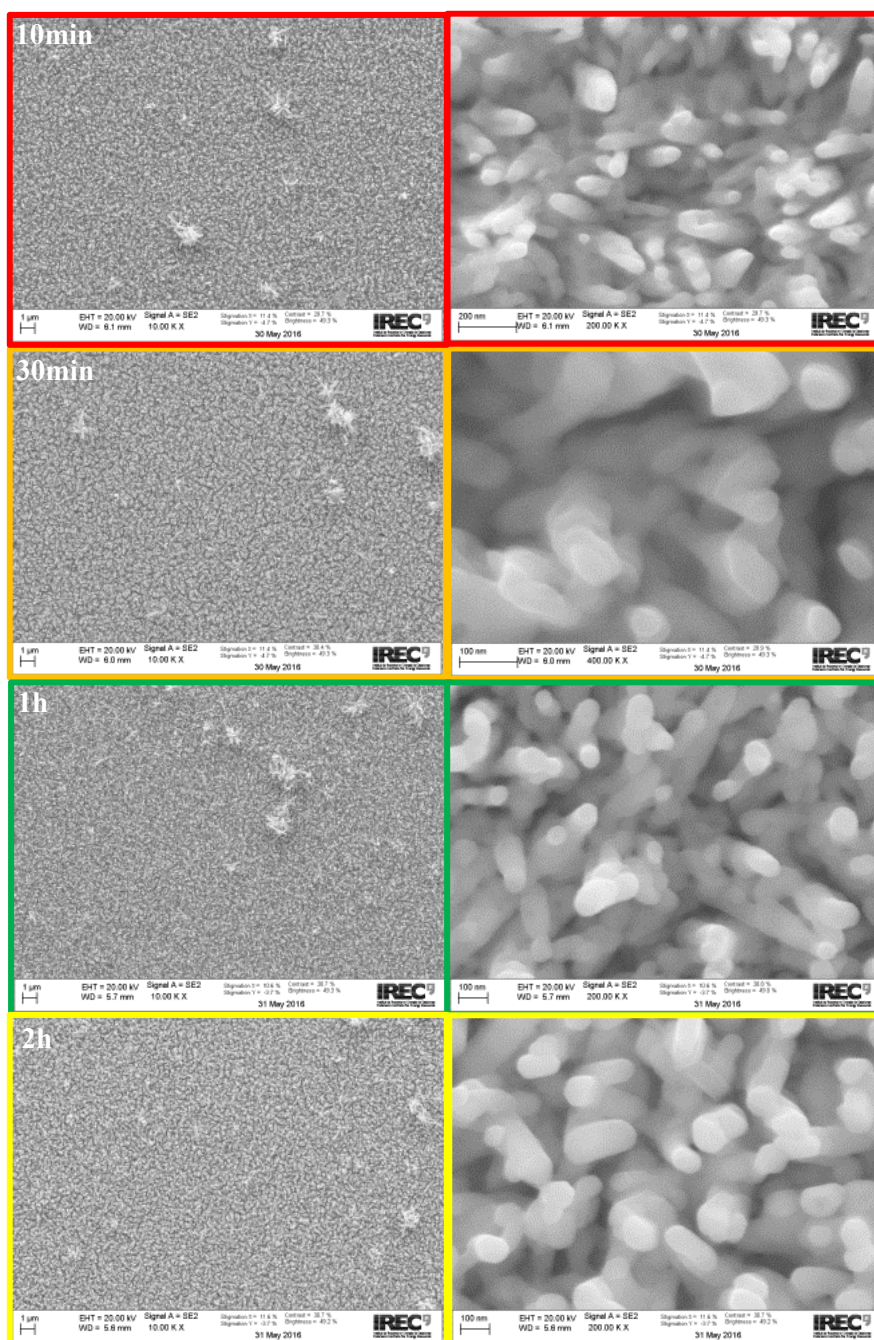


Figure S26. SEM images of the $\text{Fe}_2\text{O}_3/\text{Fe}_2\text{TiO}_5$ -30 cycles electrodes with different sintering time at 750 °C, e.g. 10 min, 30min, 1 h and 2 h.

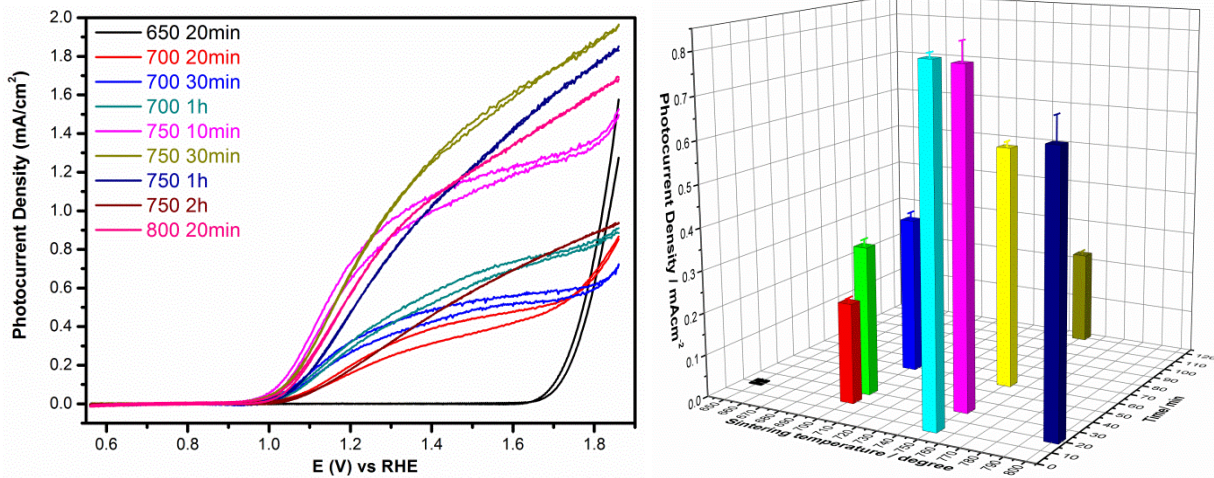
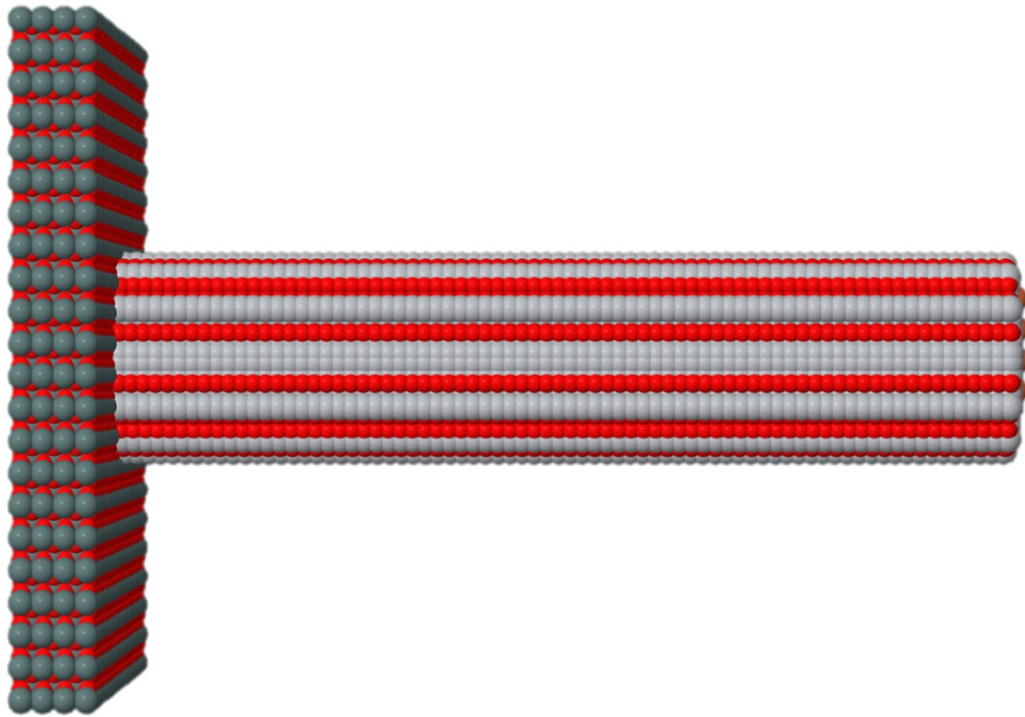
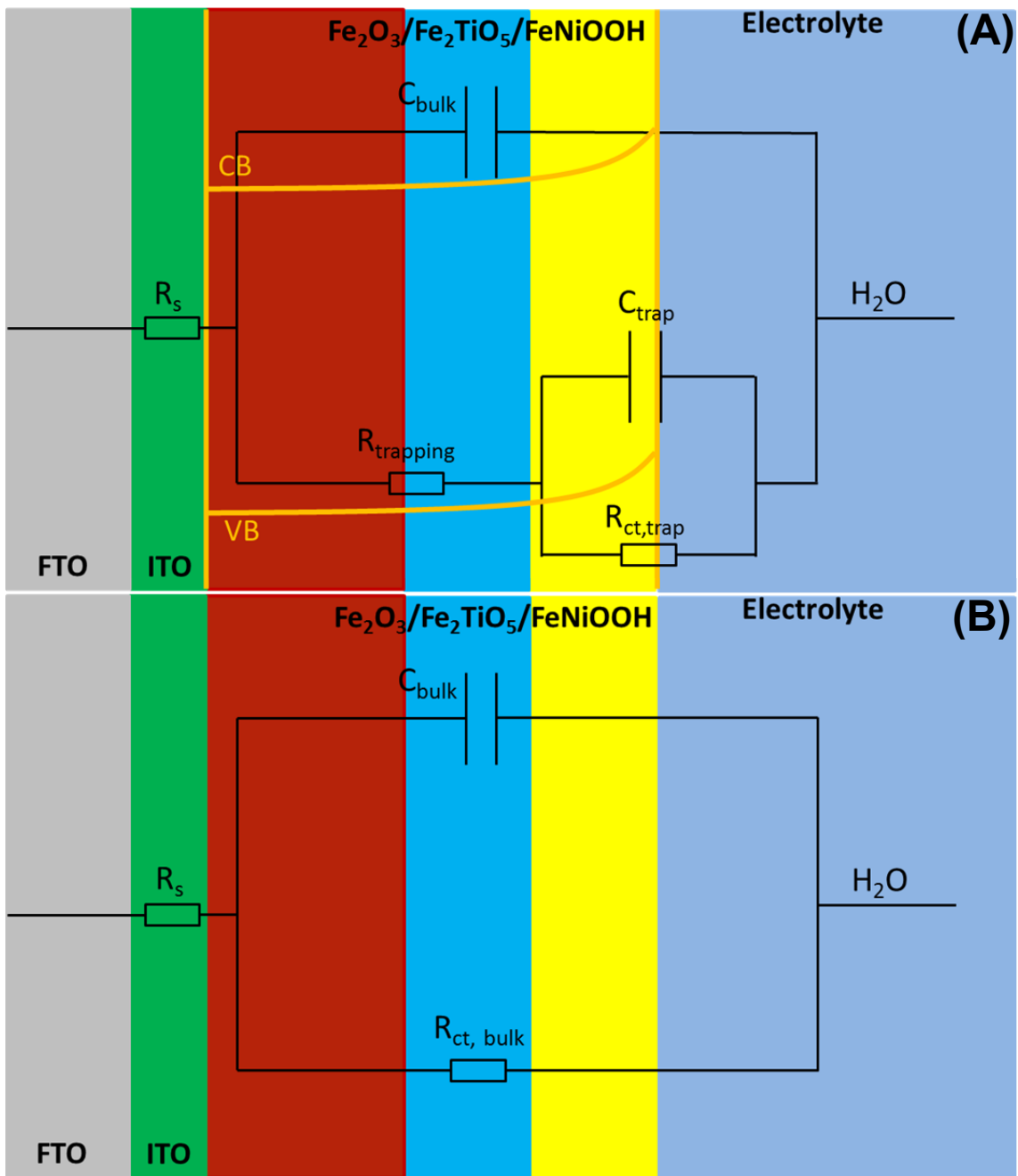


Figure S27. Top: the atomic model for the optimized $\text{Fe}_2\text{O}_3/\text{Fe}_2\text{TiO}_5$ -30 cycles electrode. Bottom: Left: CV curves of the $\text{Fe}_2\text{O}_3/\text{Fe}_2\text{TiO}_5$ -30 cycles electrodes with different sintering conditions under illumination; Right: the photocurrent density at 1.23 V vs. RHE related to the sintering conditions (the error bar stemmed from the standard deviation of statistic data collected at least three repeated electrodes).

As a proof of the necessity of ITO underlayer between FTO substrate and $\text{Fe}_2\text{O}_3/\text{Fe}_2\text{TiO}_5$ nanowires, the $\text{Fe}_2\text{O}_3/\text{Fe}_2\text{TiO}_5$ -30 cycles electrode was also fabricated and the sintering condition has been optimized, as presented in Figures S26 and S27. According to Figure S27, the optimization sintering condition for the $\text{Fe}_2\text{O}_3/\text{Fe}_2\text{TiO}_5$ -30 cycles electrode is 750°C for 30 min and the corresponding photocurrent is 0.81 mA cm^{-2} , which is much lower than 1.56 mA cm^{-2} of the ITO/ $\text{Fe}_2\text{O}_3/\text{Fe}_2\text{TiO}_5$ -30 cycles electrode and thus further confirm the beneficial function of the ITO underlayer.



Schematic S1. A: Equivalent circuit (EC) for the charge transfer process of hematite composite under illumination, the hematite composite/electrolyte interface is mediated by surface states. R_s , resistance associated with the electric contacts of the electrode, electrolyte, etc. R_{trapping} , resistance associated with charge trapping at surface states. C_{bulk} , capacitance associated with charge accumulation in the bulk. $R_{\text{ct, trap}}$, resistance associated with the charge transfer process from surface states. C_{trap} , capacitance associated with charge accumulation on the surface states. B: simple Randles circuit for the charge transfer process of hematite composite under dark. R_s , resistance associated with the electric contacts of the electrode, electrolyte, etc. In this case, the $C_{\text{ct, trap}}$ and R_{ct} are eliminated because there is no surface states mediated process under dark.

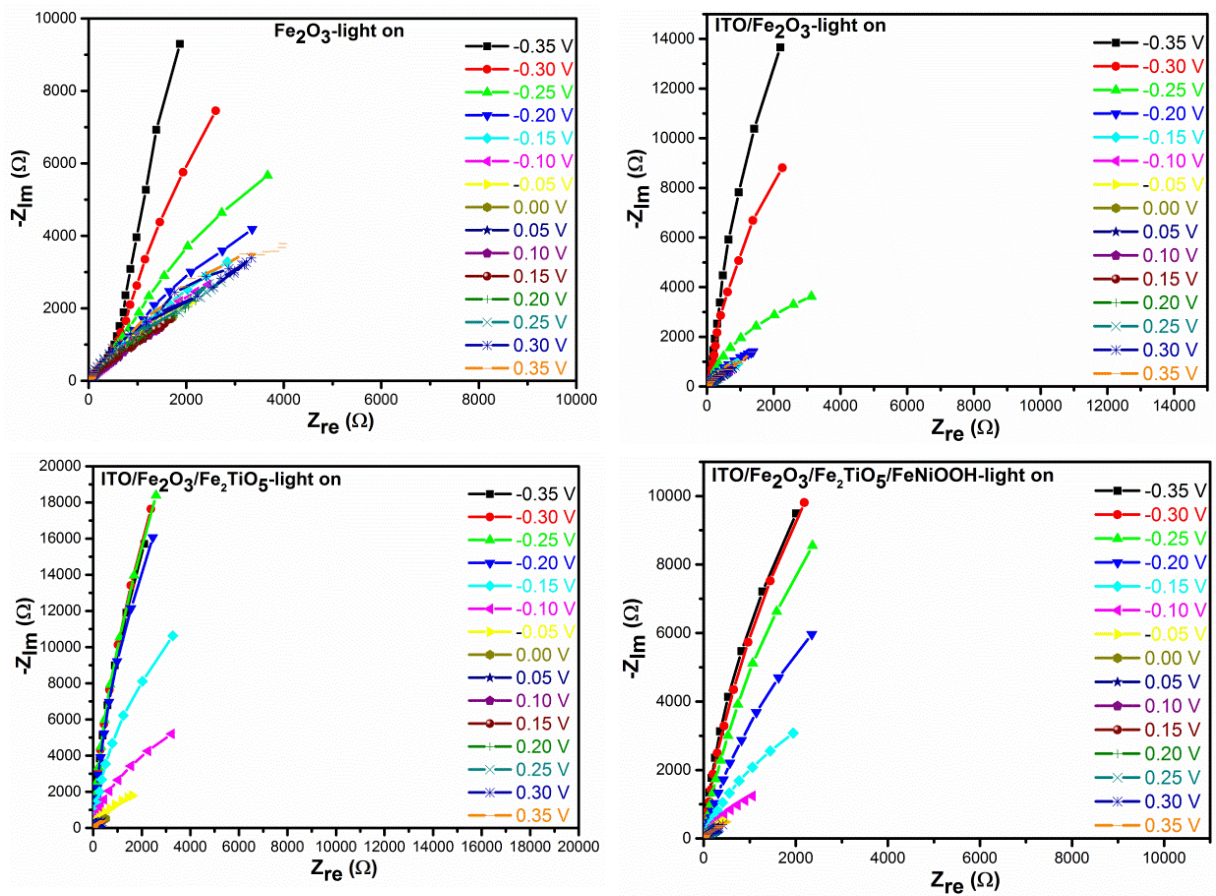


Figure S28. Nyquist (Imaginary vs. Real component of impedance) plots under light illumination of the Fe_2O_3 , ITO/ Fe_2O_3 , ITO/ Fe_2O_3 / Fe_2TiO_5 , and ITO/ Fe_2O_3 / Fe_2TiO_5 / FeNiOOH electrodes at -0.35, -0.3, -0.25, -0.2, -0.15, -0.10, -0.05, 0.00, 0.05, 0.10, 0.15, 0.20, 0.25, 0.30 and 0.35 V vs Ag/AgCl reference electrode. (Electrolyte: 1 M NaOH. AC amplitude: 5 mV. Frequency range: 100 mHz - 1MHz.)

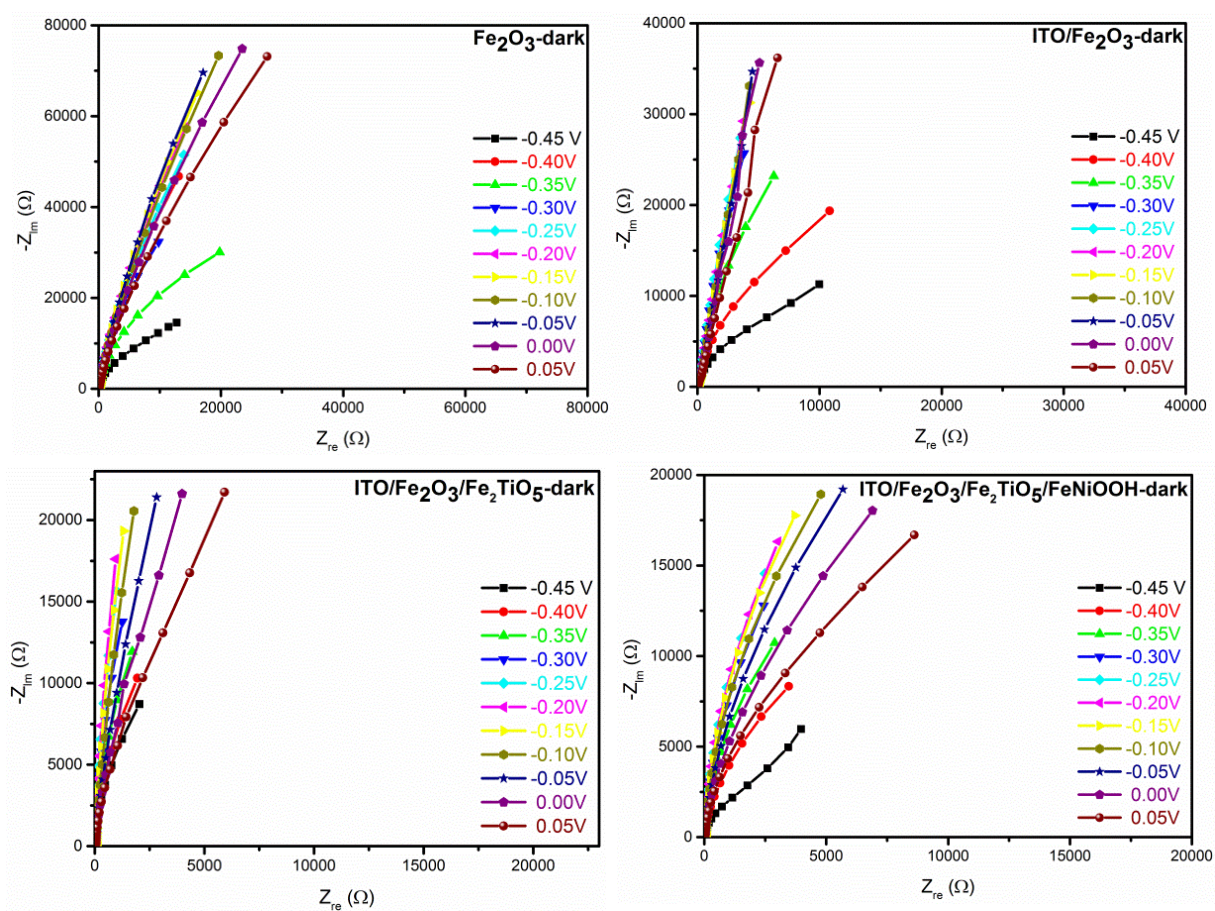


Figure S29. Nyquist (Imaginary vs. Real component of impedance) plots in the dark of the Fe_2O_3 , ITO/ Fe_2O_3 , ITO/ Fe_2O_3 / Fe_2TiO_5 , and ITO/ Fe_2O_3 / Fe_2TiO_5 / $FeNiOOH$ electrodes at -0.45, -0.4, -0.35, -0.3, -0.25, -0.2, -0.15, -0.10, -0.05, 0.00 and 0.05 V vs Ag/AgCl reference electrode. (Electrolyte: 1 M NaOH. AC amplitude: 5 mV. Frequency range: 100 mHz - 1MHz.)

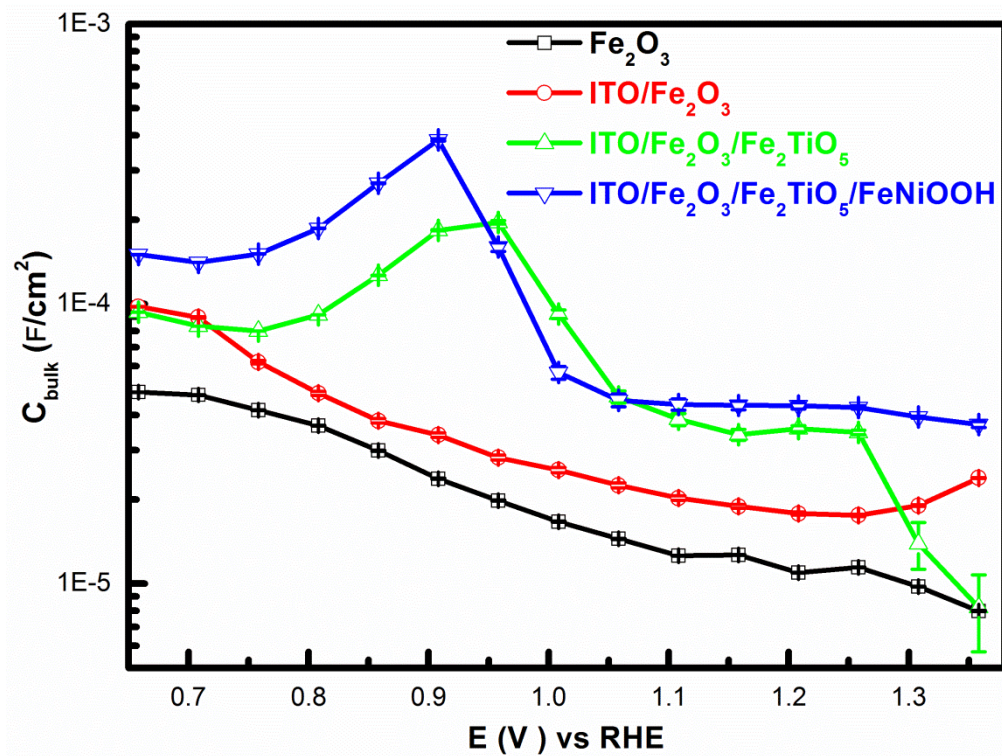


Figure S30. C_{bulk} of the Fe_2O_3 , $\text{ITO}/\text{Fe}_2\text{O}_3$, $\text{ITO}/\text{Fe}_2\text{O}_3/\text{Fe}_2\text{TiO}_5$, and $\text{ITO}/\text{Fe}_2\text{O}_3/\text{Fe}_2\text{TiO}_5/\text{FeNiOOH}$ electrodes as a function of the applied potential obtained from fitting EIS data in contact with 1M NaOH electrolytes under 1 sun illumination. Error bars stem from the goodness of the EIS data fittings.

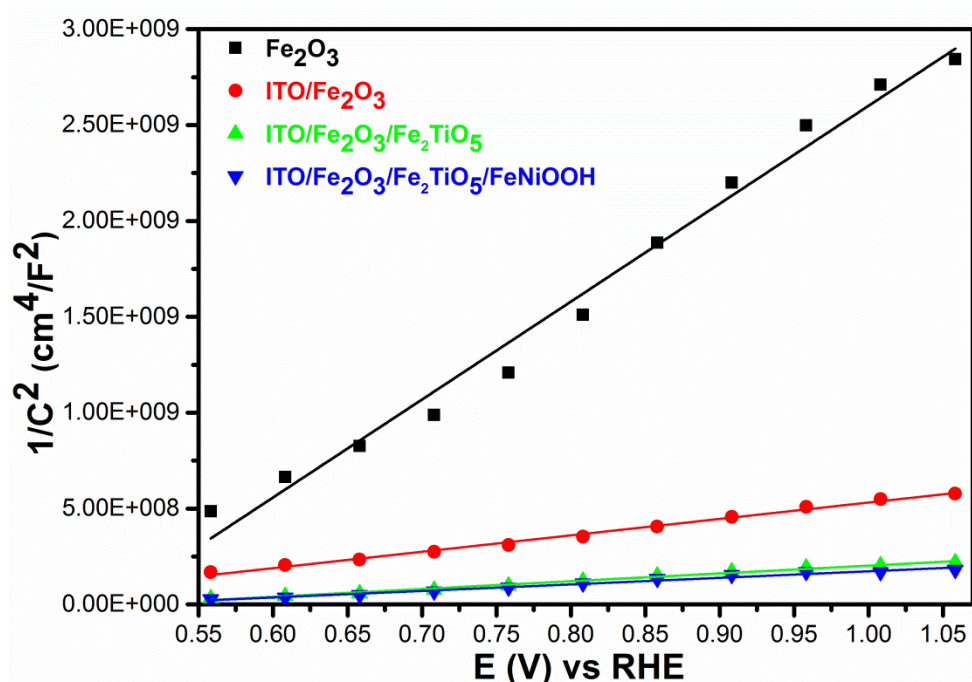


Figure S31. Mott-Schottky plots (C^{-2} vs. E) of the Fe_2O_3 , ITO/ Fe_2O_3 , ITO/ $\text{Fe}_2\text{O}_3/\text{Fe}_2\text{TiO}_5$, and ITO/ $\text{Fe}_2\text{O}_3/\text{Fe}_2\text{TiO}_5/\text{FeNiOOH}$ electrodes. Each point was obtained upon fitting the corresponding Nyquist plot at each potential in the dark to a classic Randles circuit (i.e. resistance and capacitance in parallel). Linear fittings (obtained in the 0.55-1.05 V vs. RHE potential range) are also depicted on each case. Electrolyte: 1 M NaOH. AC amplitude: 5 mV. Frequency range: 100 mHz - 1 MHz.

In order to gain further information on the bulk of hematite nanowires, impedance measurements were performed in the dark to derive the corresponding Mott-Schottky plots. Upon fitting the Nyquist plots to a Randles circuit (Schematic 1B), the potential-dependent capacitances were plotted following the Mott-Schottky model (C^{-2} vs. E , Fig. S31). When this model holds, equation (1) is used to fit the plots:⁶

$$\frac{1}{C^2} = \frac{2}{e\epsilon\epsilon_r N_D} \left(E - E_{fb} - \frac{kT}{e} \right) \quad (1)$$

where N_D is the charge donor density (cm^{-3}), E_{fb} is the flat band potential (V), ϵ is the vacuum permittivity ($8.85 \times 10^{-12} \text{ F m}^{-1}$), ϵ_r is the relative dielectric constant of hematite ($\epsilon_r = 32$), k is the Boltzmann constant ($1.38 \times 10^{-23} \text{ J K}^{-1}$) and T is the absolute temperature (K).

Table S1. Flat band potential values (E_{fb}), bulk donor densities (N_D) and total surface state density (N_{ss}) of the Fe_2O_3 , ITO/ Fe_2O_3 , ITO/ $\text{Fe}_2\text{O}_3/\text{Fe}_2\text{TiO}_5$, and ITO/ $\text{Fe}_2\text{O}_3/\text{Fe}_2\text{TiO}_5/\text{FeNiOOH}$ electrodes. E_{fb} and N_D values were respectively estimated from the x-intercepts (at $C^{-2} = 0$) and slopes of the Mott-Schottky plots (Figure S31).

Samples	N_D/cm^{-3}	$E_{fb}/\text{V vs. RHE}$	N_{ss}/cm^{-2}
Fe_2O_3	4.60E+18	0.465	9.53E+14
ITO/ Fe_2O_3	2.75E+19	0.353	1.54E+15
ITO/ $\text{Fe}_2\text{O}_3/\text{Fe}_2\text{TiO}_5$	5.80E+19	0.475	2.17E+15
ITO/ $\text{Fe}_2\text{O}_3/\text{Fe}_2\text{TiO}_5/\text{FeNiOOH}$	6.89E+19	0.468	1.23E+16

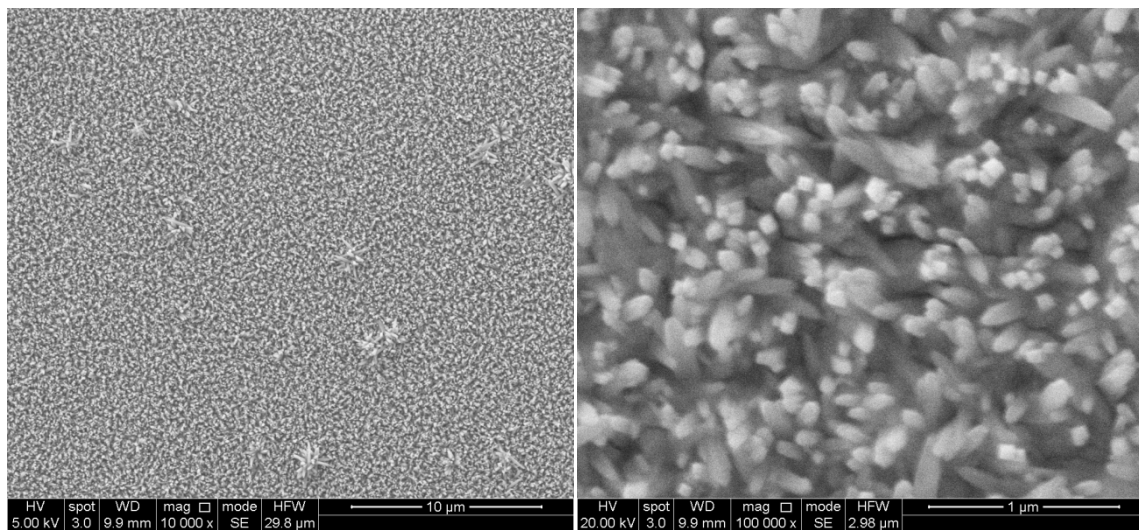


Figure S32. SEM images of FeOOH nanowires on FTO substrate.

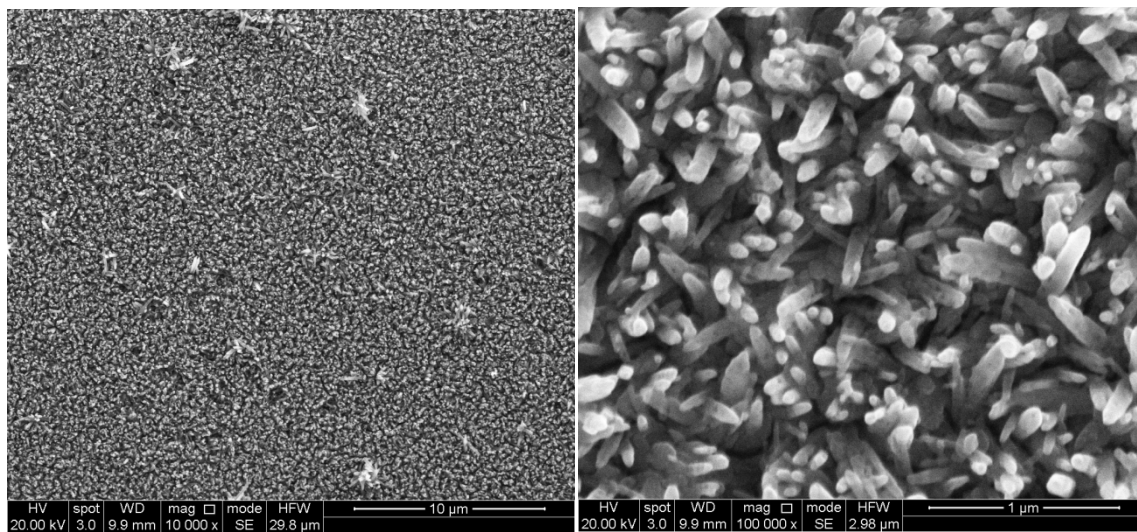
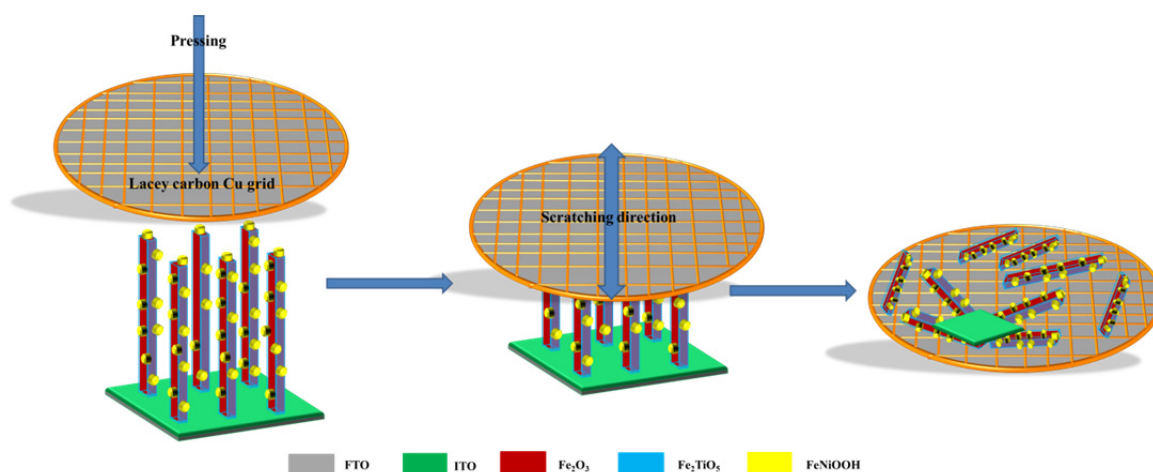


Figure S33. SEM images of FeOOH nanowires on FTO substrate after sintering at 550°C for 2h.



Schematic S2 The sample preparation process of FTO/ITO/Fe₂O₃/Fe₂TiO₅/FeNiOOH electrode for TEM and STEM-EELS characterization.

In order to avoid the chemical contamination from the solvent (ethanol, hexane etc.) and intensive mechanical damage (ultrasonic dispersion) during the TEM sample preparation, we directly scratched these nanowires from the as-prepared electrode. As displayed in schematic S2, the fragile nanowires were scratched and dispersed randomly on a lacey carbon Cu grid. It should be pointed out that some of the scratched nanowires disconnect from the ITO matrix, meanwhile other nanowires were still adhered to the ITO matrix.

Table S2. Photoelectrochemical performance comparison of hematite based electrodes.

Reference no.	Materials	Fabrication methods	Photocurrent at 1.23 V vs RHE (mA/cm ²)
[6]	Fe ₂ O ₃ /Fe ₂ TiO ₅	Sol-gel	1.35
[12]	Fe ₂ O ₃ /molecular Ir catalyst	Hydrothermal, soaking reaction	0.66
[13]	Fe ₂ O ₃ /NiO _x	Hydrothermal, photoelectrodeposition	0.6
[14]	Fe ₂ O ₃ /Fe-Pi	Hydrothermal, furnace heating	0.8
[15]	Fe ₂ O ₃ /TiO ₂	Hydrothermal, CBD	1.3
[16]	Fe ₂ O ₃ /graphene	Hydrothermal, CBD	0.5
[17]	Fe ₂ O ₃	Hydrothermal	0.8
[18]	C/Co ₃ O ₄ -Fe ₂ O ₃	Hydrothermal, electrodeposition	1.48
[19]	Fe ₂ O ₃ /TiO ₂	Thermal oxidation, lithography	0.45
[20]	Mesoporous Fe ₂ O ₃	Chemical etching	0.61
[21]	Fe ₂ O ₃ film	Spray pyrolysis	0.65
[22]	Fe ₂ O ₃ /FeOOH	PLD, photodeposition	0.85
[23]	TiO ₂ /Fe ₂ O ₃ /Ni(OH) ₂	ALD, hydrothermal, dipping	0.3
[24]	Fe ₂ O ₃ /TiO _x /FeOOH	Hydrothermal, electrodeposition	1.5
[25]	Co-N _x P doped carbon/graphene/Fe ₂ O ₃	Hydrothermal, chemical bath	2.15
[26]	Acid etched Fe ₂ O ₃	Chemical etching	1.0
[27]	Fe ₂ O ₃ /FeOOH	Hydrothermal, chemical bath	1.21
[28]	Fe ₂ O ₃ /TiO ₂	PE-CVD, ALD	1.8
[29]	Fe ₂ O ₃ /ZrO ₂ /Co-Pi	Hydrothermal, ALD, photo-electrodeposition	1.87
[30]	Fe ₂ O ₃ /IrO _x	Hydrothermal, Soaking	0.7
[31]	Fe ₂ O ₃	Electrodeposition	1.0
[32]	Fe ₂ O ₃ /Fe ₂ TiO ₅	Hydrothermal	1.4
[33]	Fe ₂ O ₃ /cobalt phosphate	Reactive ballistic and photo depositions	2.0
[34]	Fe ₂ O ₃ /NiO _x	Hydrothermal, photodeposition	0.6
[35]	Fe ₂ O ₃ /SiO ₂ /Sn doping	Hydrothermal, Chemical bath	2.0
Our work	ITO/Fe ₂ O ₃ /Fe ₂ TiO ₅ /FeNiOOH	Sputtering, Hydrothermal, ALD, photoelectrodeposition	2.20

References:

- [1] Q. H. Liu, J. F. He, T. Yao, Z. H. Sun, W. R. Cheng, S. He, Y. Xie, Y. H. Peng, H. Cheng, Y. F. Sun, Y. Jiang, F. C. Hu, Z. Xie, W. S. Yan, Z. Y. Pan, Z. Y. Wu, S. Q. Wei, *Nature Communications*, 2014, **5**, 5122.
- [2] J. Y. C. Chen, L. N. Dang, H. F. Liang, W. L. Bi, J. B. Gerken, S. Jin, E. E. Alp, S. S. Stahl, *J. Am. Chem. Soc.* 2015, **137**, 15090-15093.
- [3] F. Y. Ning, M. F. Shao, S. M. Xu, Y. Fu, R. K. Zhang, M. Wei, D. G. Evans, X. Duan, *Energy Environ. Sci.*, 2016, **9**, 2633-2643.
- [4] M. Görlin, P. Chernev, J. F. d. Araújo, T. Reier, S. Dresch, B. Paul, R. Krähnert, H. Dau, P. Strasser, *J. Am. Chem. Soc.* 2016, **138**, 5603-5614.
- [5] D. Friebe, M. W. Louie, M. Bajdich, K. E. Sanwald, Y. Cai, A. M. Wise, M.J. Cheng, D. Sokaras, T. C. Weng, R. Alonso-Mori, R. C. Davis, J.R. Bargar, J. K. Nørskov, A. Nilsson, A. T. Bell, *J. Am. Chem. Soc.* 2015, **137**, 1305-1313.
- [6] D. M. Satoca, M. Bartsch, C. Fabrega, A. Genç, S. Reinhard, T. Andreu, J. Arbiol, M. Niederberger, J. R. Morante, *Energy Environ. Sci.*, 2015, **8**, 3242-3254.
- [7] L. J. Han, P. Y. Tang, A. Reyes-Carmona, B. Rodriguez-Garcia, M. Torrens, J. R. Morante, J. Arbiol, J. R. Galan-Mascaros, *J. Am. Chem. Soc.*, 2016, **138**, 16037-16045.
- [8] F. Song, X. Hu, *Nat. Commun.* 2014, **5**, 4477.
- [9] Y. Zhao, X. Jia, G. Chen, L. Shang, G. I. Waterhouse, L. Z. Wu, C. H. Tung, D. O'Hare, T. Zhang, *J. Am. Chem. Soc.* 2016, **138**, 6517-6524.
- [10] T. W. Kim, K. S. Choi, *Science*, 2014, **343**, 990-994.
- [11] L. Wang, F. Dionigi, N. T. Nguyen, R. Kirchgeorg, M. Glieth, S. Grigorescu, P. Strasser, P. Schmuki, *Chem. Mater.* 2015, **27**, 2360-2366.
- [12] W. Li, S.W. Sheehan, D., Y. He, X. Yao, R. L. Grimm, G. W. Brudvig, D. W. Wang, *Angew. Chem. Int. Ed.* 2015 **54**, 11428-11432.
- [13] F. Malara, F. Fabbri, M. Marelli, A. Naldoni, *ACS Catal.* 2016, **6**, 3619-3628.
- [14] Z. F. Hu, Z. R. Shen, J. C. Yu, *Chem. Mater.* 2016, **28**, 564-572.
- [15] Y. G. Li, X. L. Wei, B. W. Zhu, H. Wang, Y. X. Tang, T. C. Sum, X. D. Chen, *Nanoscale*, 2016, **8**, 11284-11290.
- [16] S. X. Liu, L. X. Zheng, P. P. Yu, S. C. Han, X. S. Fang, *Adv. Funct. Mater.* 2016, **26**, 3331-3339.
- [17] Y. C. Zhang, H. N. Zhang, H. W. Ji, W. H. Ma, C. C. Chen, J. C. Zhao, *J. Am. Chem. Soc.*, 2016, **138**, 2705-2711.
- [18] P. Zhang, T. Wang, X.X. Chang, L. Zhang, J. L. Gong, *Angew. Chem. Int. Ed.* 2016, **55**, 5851-5855.
- [19] B. Iandolo, B. Wickman, E. Svensson, D. Paulsson, Anders Hellman, *Nano Lett.*, 2016, **16**, 2381-2386.
- [20] C. W. Wang, S. Yang, W. Q. Fang, P. Liu, H. J. Zhao, H. G. Yang, *Nano Lett.*, 2016, **16**, 427-433.
- [21] P. Dias, A. Vilanova, T. Lopes, L. Andrade, A. Mendes, *Nano Energy*, 2016, **23**, 70-79.
- [22] Q. Yu, X. G. Meng, T. Wang, P. Li, J. H. Ye, *Advanced Functional Materials*, 2015, **25**, 2686-2692.
- [23] L. Steier, J.S. Luo, M. Schreier, M. T. Mayer, T. Sajavaara, M. Grätzel, *ACS Nano*, 2015, **9**, 11775-11783.
- [24] I. S. Cho, H. S. Han, M. Logar, J. Park, X. L. Zheng, *Adv. Energy Mater.* 2015, 1501840.
- [25] Y. Hou, M. Qiu, T. Zhang, J. Ma, S. H. Liu, X. D. Zhuang, C. Yuan, X. L. Feng, *Advanced Materials*, 2017, **29**, 1604480.
- [26] Y. Yang, M. Forster, Y.C. Ling, G.M. Wang, T. Zhai, Y.X. Tong, A. J. Cowan, Y. Li, *Angew. Chem. Int. Ed.*, 2016, **55**, 3403-3407.
- [27] J. Y. Kim, D. H. Youn, K. Kang, J. S. Lee, *Angew. Chem. Int. Ed.*, 2016, **55**, 10854-10858.
- [28] A. Mettenbörgera, Y. Gönüllüa, T. Fischera, T. Heisiga, A. Sasinskaa, C. Maccatob, G. Carrarob, C. Sadac, D. Barrecad, L. Mayrhofer, M. Moselere, A. Helde, S. Mathur, *Nano Energy*, 2016, **19**, 415-427.
- [29] C. C. Li, A. Li, Z. B. Luo, J. J. Zhang, X. X. Chang, Z. Q. Huang, T. Wang, J. L. Gong, *Angew. Chem. Int. Ed.*, 2017, **56**, 4214-4219.
- [30] W. Li, D. He, S. W. Sheehan, Y.M. He, J. E. Thorne, X.H. Yao, G. W. Brudvig, D.W. Wang, *Energy Environ. Sci.*, 2016, **9**, 1794-1802.
- [31] O. Zandi, A. R. Schon, H. Hajibabaei, T.W. Hamann, *Chem. Mater.*, 2016, **28**, 765-771.
- [32] P. S. Bassi, R. P. Antony, P. P. Boix, Y.N. Fang, J. Barber, L. H. Wong, *Nano Energy*, 2016, **22**, 310-318.
- [33] Z.B. Luo, C.C. Li, S. S. Liu, T. Wang, J. L. Gong, *Chem. Sci.*, 2017, **8**, 91-100.
- [34] F. Malara, F. Fabbri, M. Marelli, A. Naldoni, *ACS Catal.* 2016, **6**, 3619-3628.
- [35] M. Y. Li, Y. Yang, Y. C. Ling, W. T. Qiu, F.X. Wang, T. Y. Liu, Y. Song, X. X. Liu, P. P. Fang, Y. X. Tong, Y. Li, *Nano Lett.*, 2017, **17**, 2490-2495.